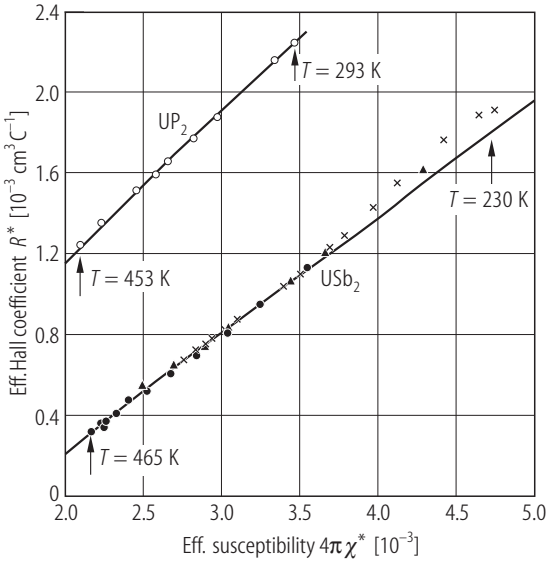

Fig. 306. UX_2, X = P, Sb, sc. Effective Hall coefficient, R^*, measured in the temperature range 230…465 K, with the current flowing in the (*ab*)-plane, vs. effective magnetic susceptibility, $\chi^* = \dfrac{\chi}{1+4\pi\chi\Theta_p}$, where χ is the volume susceptibility [91HWFM]. Open circles: UP_2; other symbols: three different samples of USb_2. The solid lines are fits to the function: $R^* = R_o + 4\pi R_s\chi^*$ (χ^* based on the data by [79TZ1]) with the parameters: $R_o = -2.8 \cdot 10^{-4}$ cm^3/C and $R_s = 0.73$ cm^3/C for UP_2, and $R_o = -9.4 \cdot 10^{-4}$ cm^3/C and $R_s = 0.58$ cm^3/C for USb_2. In a single band approximation the normal Hall coefficients, R_o, yield the Hall carrier concentrations per U atom $n_H = 2.2 \cdot 10^{22}$ and $6.6 \cdot 10^{21}$ cm^{-3} for UP_2 and USb_2, respectively. Note that the spontaneous Hall coefficient, R_s, is positive and about three orders of magnitude higher than R_o. The earlier results for UP_2 were $R_o = -3 \cdot 10^{-4}$ cm^3/C and $R_s = 2.3$ cm^3/C [69HT].

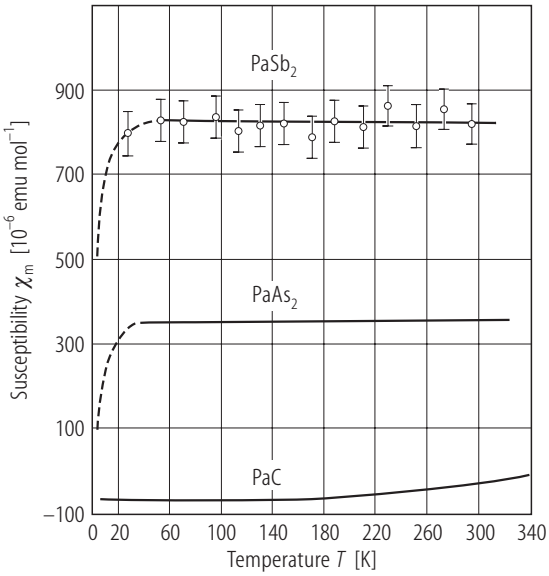

Fig. 307. PaX_2, X = As, Sb. Molar magnetic susceptibility, χ_m, vs. temperature, T [79HDC]. For comparison there is shown $\chi_m(T)$ of diamagnetic PaC. Both PaX_2 compounds are temperature independent paramagnets with the susceptibility of $0.34 \cdot 10^{-3}$ and $0.82 \cdot 10^{-3}$ emu/mol for $PaAs_2$ and $PaSb_2$, respectively, as compared to $-0.050 \cdot 10^{-3}$ emu/mol for PaC [77HWBD]. The downturn in $\chi_m(T)$ below 30 K is probably caused by diamagnetic impurities. See also [78HDHD].

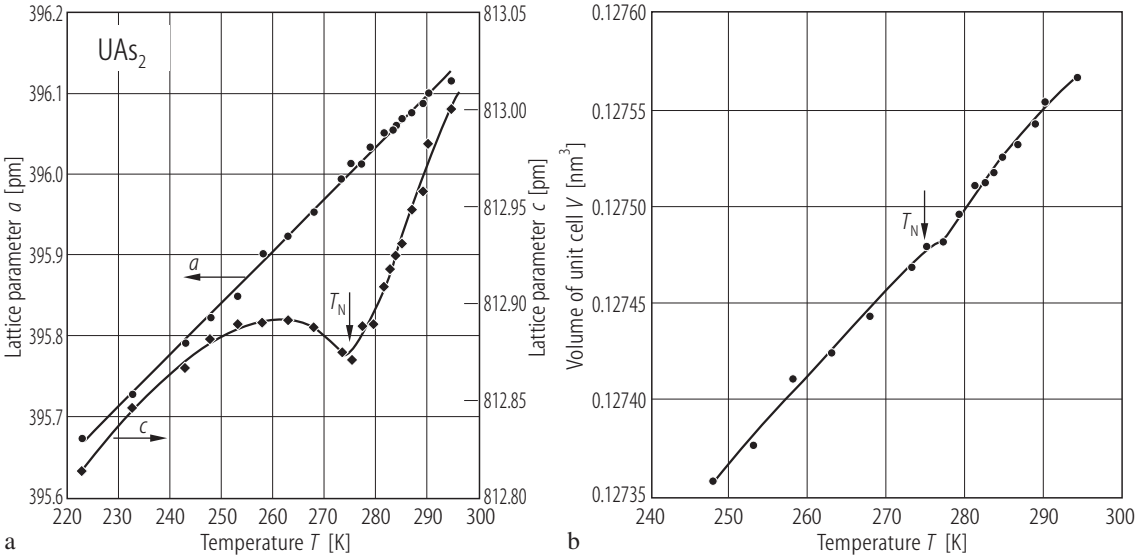

Fig. 308. UAs_2, sc. **(a)** Tetragonal lattice parameters, a and c, vs. temperature, T, in the range 220…295 K [77PL]. Note the absence of any anomaly in $a(T)$ at T_N = 273 K, whereas a sharp minimum is present in $c(T)$, which leads to a large anisotropy in the thermal expansion. **(b)** Unit cell volume, V, vs. temperature T [77LPKM]. Note that near T_N there is only a weak anomaly in $V(T)$.

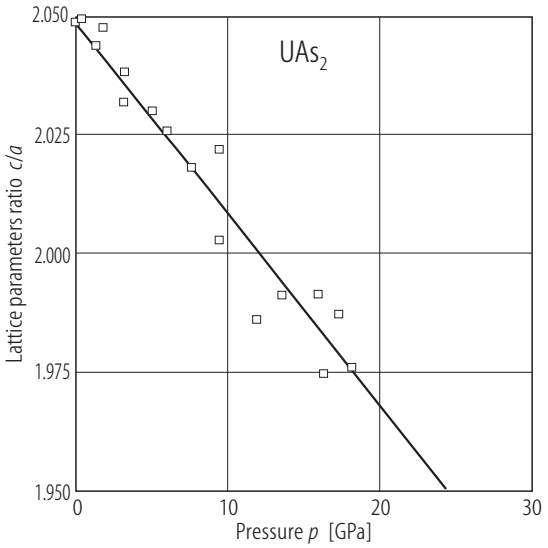

Fig. 309. UAs_2. Ratio of the lattice parameters, c/a, vs. pressure, p, up to 18 GPa [93GSBD]. The solid line serves as a guide to the eye.

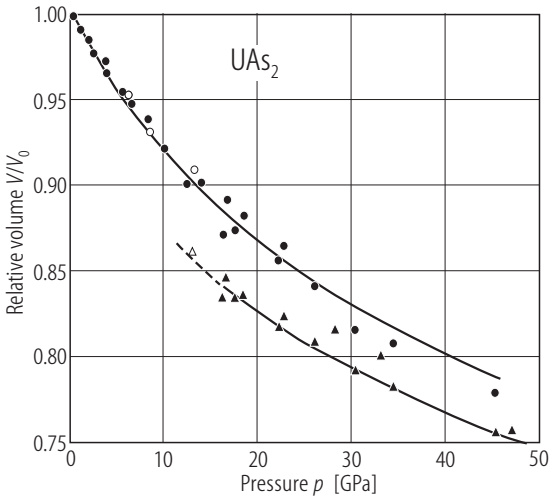

Fig. 310. UAs_2. Relative volume, V/V_0, vs. pressure, p, up to 48 GPa [90GSBD]. Circles: tetragonal phase; triangles: orthorhombic phase. Filled symbols: increasing pressure; open symbols: decreasing pressure. A first-order tetragonal-to-orthorhombic phase transformation takes place at about 15 GPa with a 4 % volume contraction. The bulk modulus B_0 = 101(8) GPa, its pressure derivative $B_0' = 4.7(7)$.

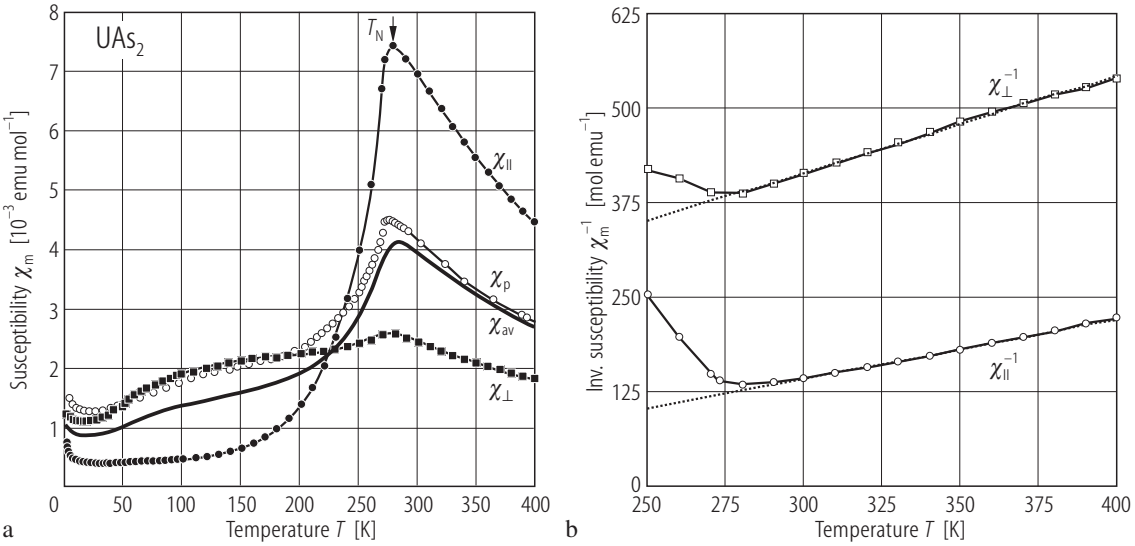

Fig. 311. UAs_2, sc. **(a)** Molar magnetic susceptibility, χ_m, vs. temperature, T, measured along the c-axis (full circles) and in the (ab)-plane (full squares) [02TSKP].]. The bold solid line represents an average molar susceptibility χ_{av} = 1/3 ($2\chi_\perp + \chi_\parallel$). For comparison the susceptibility measured on a polycrystalline sample is also shown (open circles). The compound orders antiferromagnetically at T_N = 273 K. Note a large anisotropy in the magnetic behaviour. **(b)** Inverse molar magnetic susceptibility, χ_m^{-1}, vs. T, measured as in panel **(a)** [02TSKP]. The dotted lines are Curie Weiss fits with the parameters given in Table F.

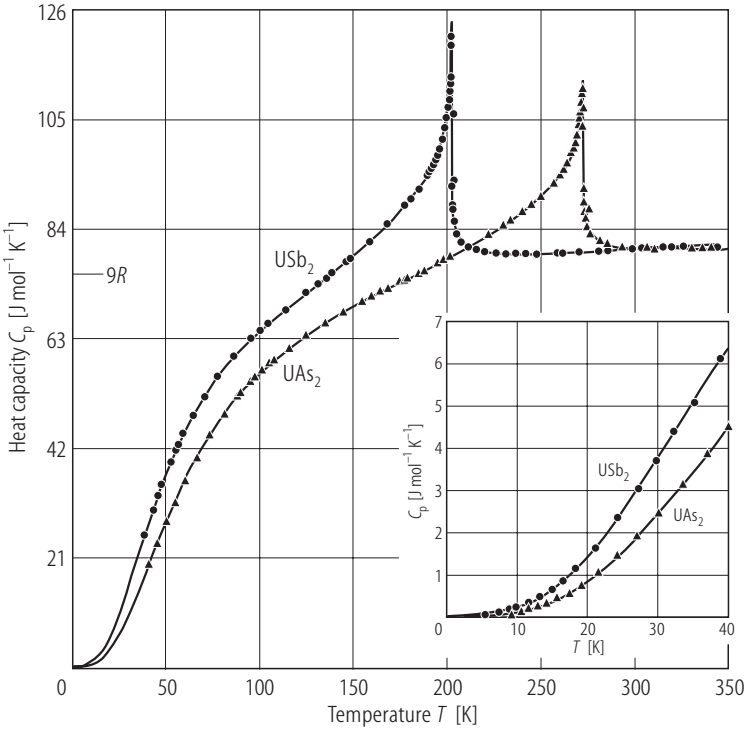

Fig. 312. UX_2, X = As, Sb. Heat capacity, C_p, vs. temperature, T, in the range 5…350 K [75WSDG]. Triangles: UAs_2; circles: USb_2. Sharp λ-shaped C_p peaks manifest second-order antiferromagnetic phase transition at T_N = 272.2 K and 202.5 K for UAs_2 and USb_2, respectively. The magnetic entropy S_{magn} is 4.142 and 7.113 J/mol K, respectively. Inset: low-temperature C_p vs. T. The electronic specific heat coefficient $\gamma(0)$ estimated from the data below 20 K is 6 and 12 mJ/mol K^2 for USb_2 and UAs_2, respectively. For comparison see the data in Fig. 285, yielding considerably different values of $\gamma(0)$.

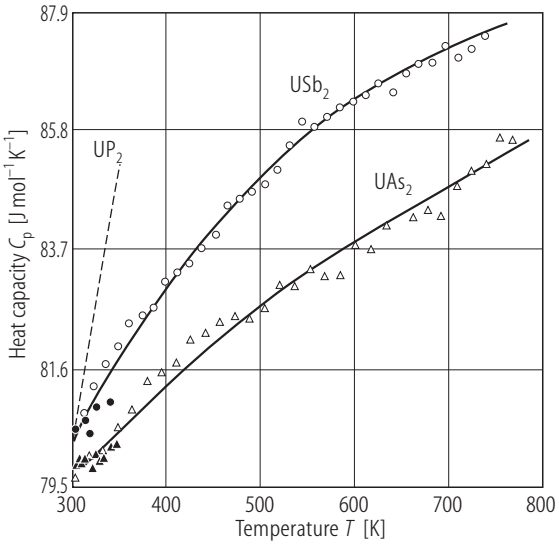

Fig. 313. UX_2, X = As, Sb. Heat capacity, C_p, vs. temperature, T, in the range 300…730 K [75WSDG]. Triangles: UAs_2; circles: USb_2. Full and open symbols denote the data obtained with different calorimeter. The dashed line represents the $C_p(T)$ data for UP_2, taken from [67SBT] (see Fig. 297). Note a pronounced difference in the magnitude and temperature variation between UP_2 and the other dipnictides. The solid lines serve as a guide for the eyes.

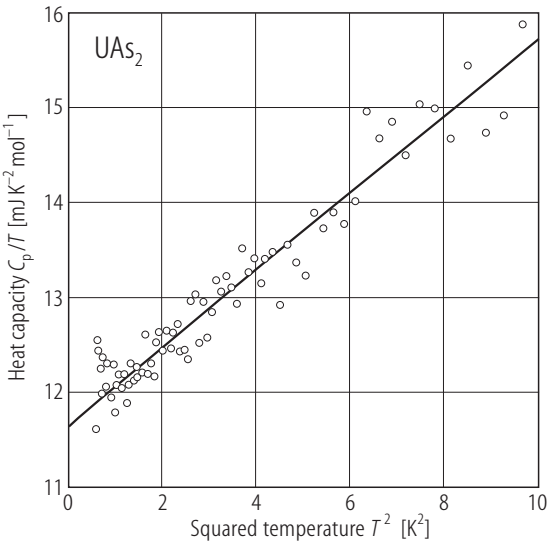

Fig. 314. UAs_2, sc. Heat capacity over temperature, C_p/T, vs. squared temperature, T^2, in the temperature range 0.7…3 K [00WAWM]. The solid line is a fit to the expression $C/T = \gamma(0) + \beta T^2$ yielding the electronic specific heat coefficient $\gamma(0) = 12$ mJ/mol K^2.

For Fig. 315 see next page

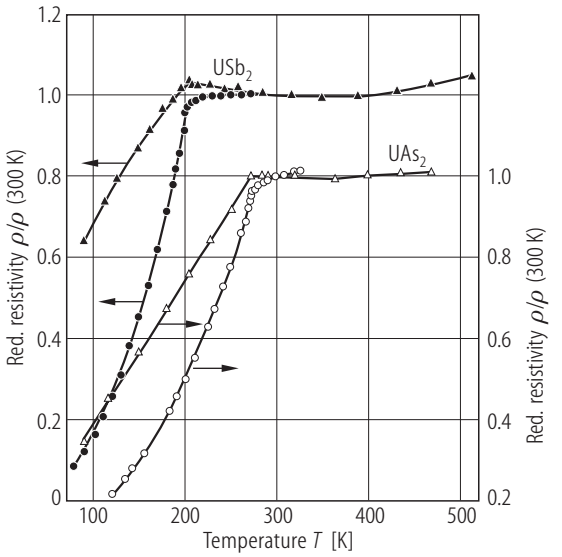

Fig. 316. UX_2, X = As, Sb, sc. Normalized electrical resistivity, $\rho/\rho(300K)$, vs. temperature, T, in the range 80…510 K measured with the current flowing in the (*ab*)-plane (circles) and on sintered samples (triangles) [72HK]. Open symbols: UAs_2 (right-hand side scale); full symbols: USb_2 (left-hand side scale). The RRR values for different single-crystalline samples varied within 200…260 for UAs_2 (compare Fig. 319) and 90…100 for USb_2 (compare Fig. 244). $\rho(300K)$ was 160 and 176 μΩcm for the arsenide and the antimonide single crystals, respectively, while for powders it was 450…500 and 550…620 μΩcm, respectively. The resistivity for sintered samples were corrected to 100% theoretical density. The difference between $\rho/\rho(300K)$ taken on single crystals and powders is caused by a strong anisotropy as is the case for UP_2 (see Fig. 299). Compare also the results for USb_2 presented in Fig. 348.

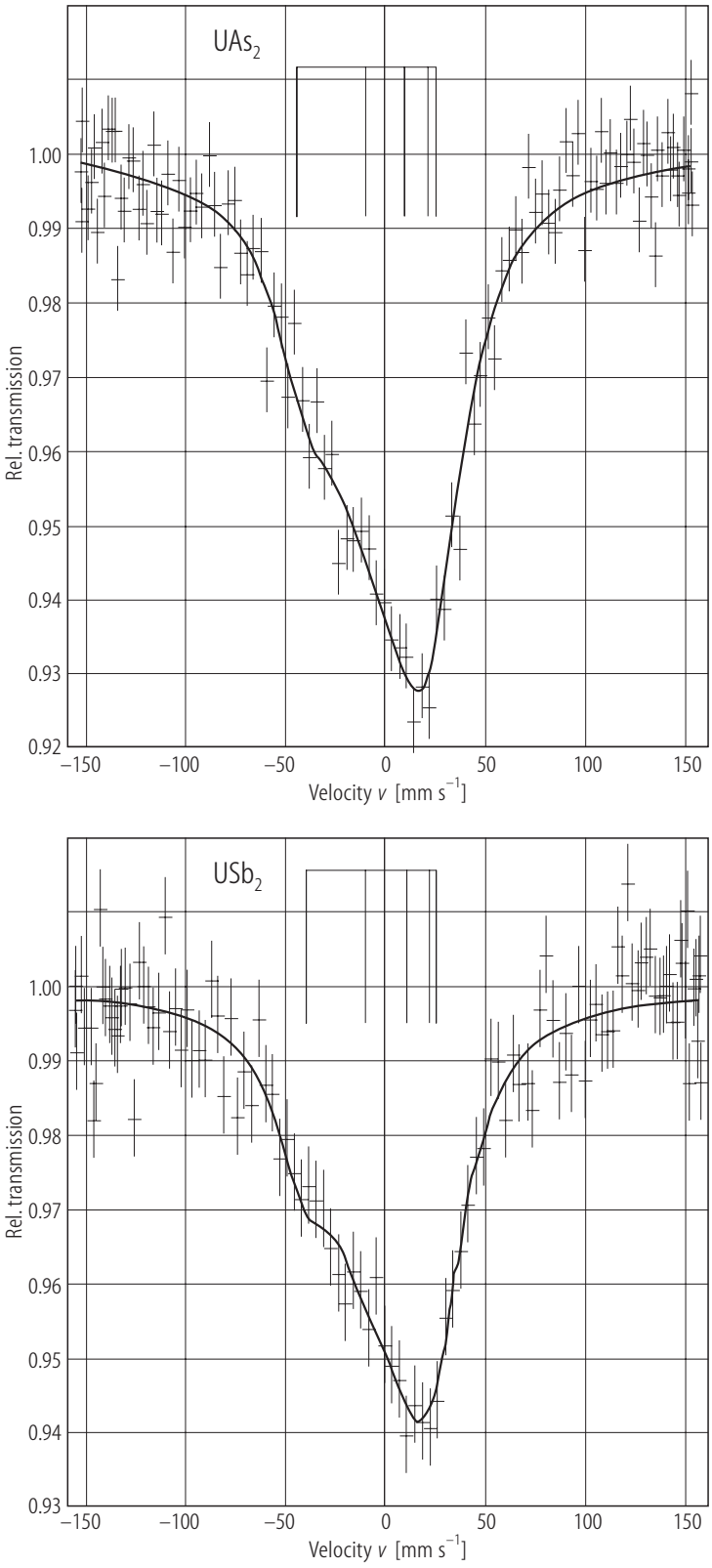

Fig. 315. UX_2, X = As, Sb. ^{238}U Mössbauer spectra taken at T = 5.3 K [01TNNH]. The combined hyperfine interactions B_{hf} have similar magnitude in both compounds being equal to about 270(20) T. From the negative nuclear quadrupolar interactions (e^2qQ = –31.3(6) and –35.4(9) mm/s for UAs_2 and USb_2, respectively) and the character of crystal and magnetic structures one can judge that the 5f orbitals in these compounds are spread within the basal plane so that the quadrupolar tensor is oblate.

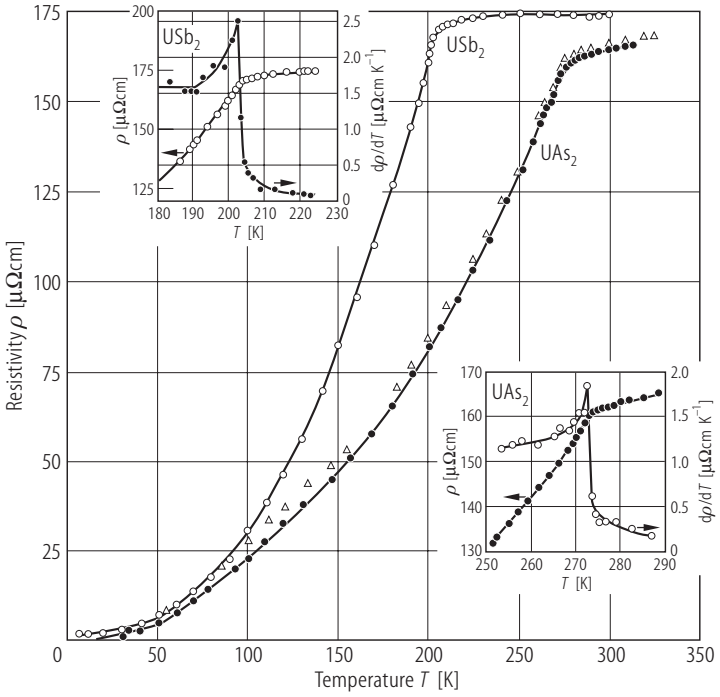

Fig. 317. UX_2, X = As, Sb, sc. Electrical resistivity, ρ, vs. temperature, T, measured with the current flowing within the (*ab*)-plane [72HK]. Triangles: UAs_2; open circles: USb_2. Several single crystals were measured with RRR in the range 200…260 for UAs_2 and 90…100 for USb_2. Full circles show $\rho(T)$ obtained on a whisker of UAs_2 (normalized to the bulk sample). Some differences between the whisker and bulk single crystal data in the intermediate temperature range is caused by little misorientation of the bulk sample resulting in the presence of the resistivity component along the *c*-axis. Insets: resistivity, ρ, and temperature derivative of the resistivity, $d\rho/dT$, vs. temperature in the vicinity of T_N. The sharp maxima in $d\rho/dT$ at the AF phase transitions in both compounds resemble the magnetic specific heat behaviour (compare Fig. 312).

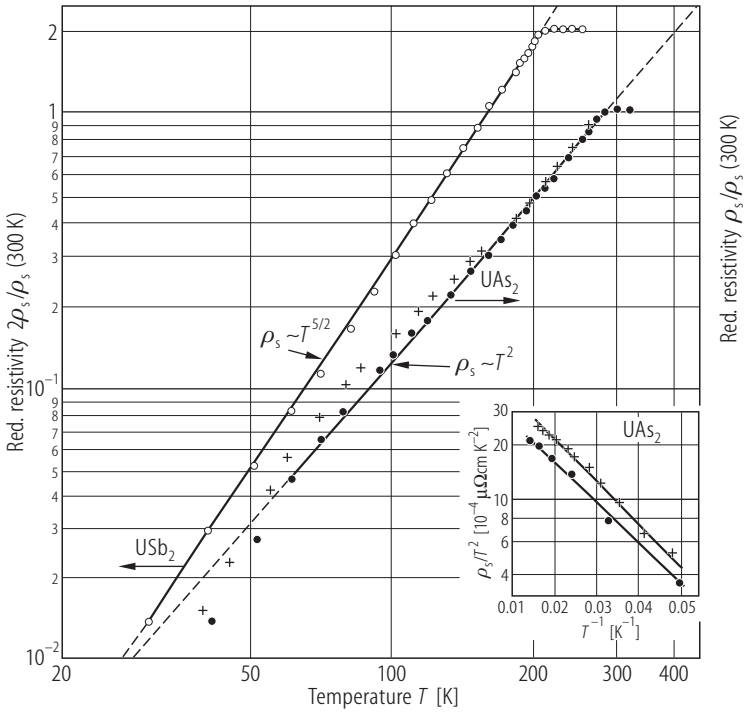

Fig. 318. UX_2, X = As, Sb, sc. Normalized spin disorder resistivity, $\rho_S/\rho_S(300K)$, vs. temperature, T, in the range 30…310 K measured with the current flowing in the (*ab*)-plane [72HK]. Note the double-logarithmic scale. Crosses: UAs_2; open circles: USb_2. Full circles show $\rho_S(T)/\rho_S(300K)$ obtained on a whisker of UAs_2 (normalized to the bulk sample). The lines indicate the $\rho_S(T) \sim T^n$ dependencies with n = 5/2 for USb_2 in the almost whole ordered region and n = 2 for UAs_2 fulfilled in the temperature range from 70 K to T_N (compare such dependencies for UP_2 and UBi_2 shown in Fig. 301). Inset: ρ_s/T^2 vs. $1/T$ for UAs_2. The solid lines mark the variation $\rho_s(T) \sim T^2\exp(-\Delta/T)$ with Δ = 51 K, which is fulfilled for UAs_2 below 60 K.

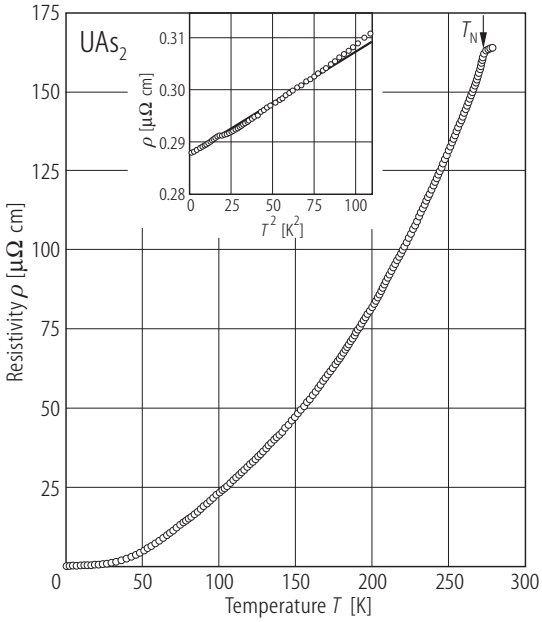

Fig. 319. UAs_2, sc. Electrical resistivity, ρ, vs. temperature, T, down to 0.1 K measured with the current flowing along the [100] direction [00WAWM]. The residual resistivity ratio $\rho(300)/\rho(0)$ is 580, and the residual resistivity is only 0.29 μΩcm, both indicating a high quality of the crystal. Note a rapid change in slope of $\rho(T)$ at the Néel temperature of 273 K. Inset: Low-temperature $\rho(T)$. The solid line marks a T^2 dependence of the resistivity below 8 K.

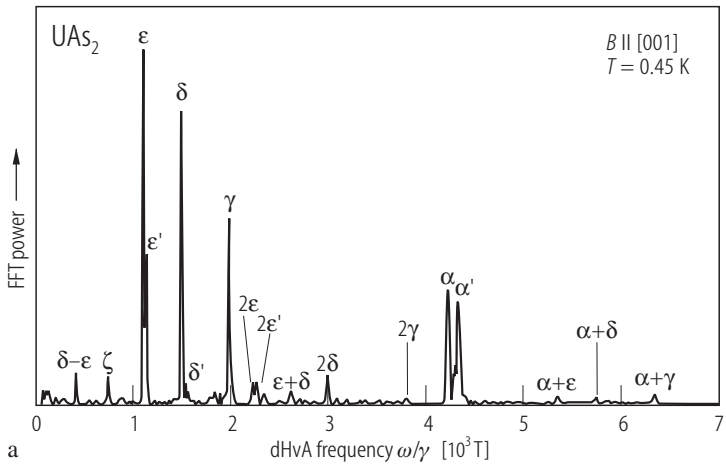

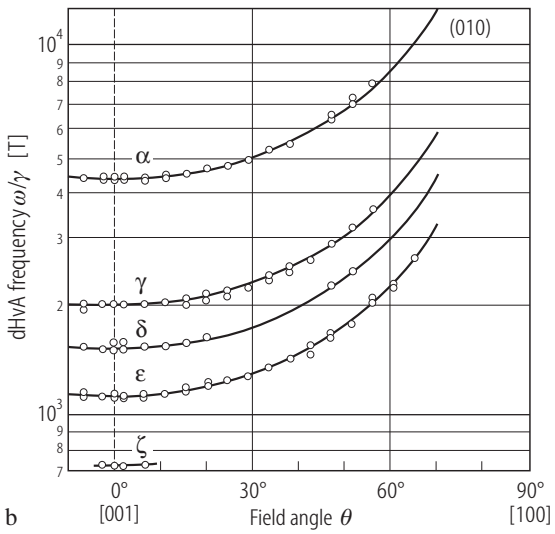

Fig. 320. UAs_2, sc. **(a)** Fast Fourier transform spectrum corresponding to the Shubnikov-de Haas oscillations measured at $T = 0.45$ K in the magnetic field ranging from 6 to 13 T applied along the [001] axis [00WAWM]. Note the presence of five fundamental branches labeled α, γ, δ, ε and ζ in the frequency range from $7.2 \cdot 10^2$ to $4.3 \cdot 10^3$ T. The other features are higher harmonics, In the original paper two additional fundamental oscillations have been reported, viz. β and η, but in the most recent analysis it was found that $\beta = 2\delta$ and $\eta = \delta - \varepsilon$ (see [00AWMW]). **(b)** Angular dependence of the SdH frequencies from panel **(a)** [00AWMW]. The solid lines mark a $1/\cos\theta$ variation which is closely followed in the case of branches α, γ, δ and ε, indicating the Fermi surface of cylindrical form (see Fig. 321). Branch ζ is observed only around [001] and it is impossible to derive the shape of corresponding Fermi surface. The effective cyclotron masses (from 0.34 to 3.1 m_0) are given in Table L. For further details see the original papers.

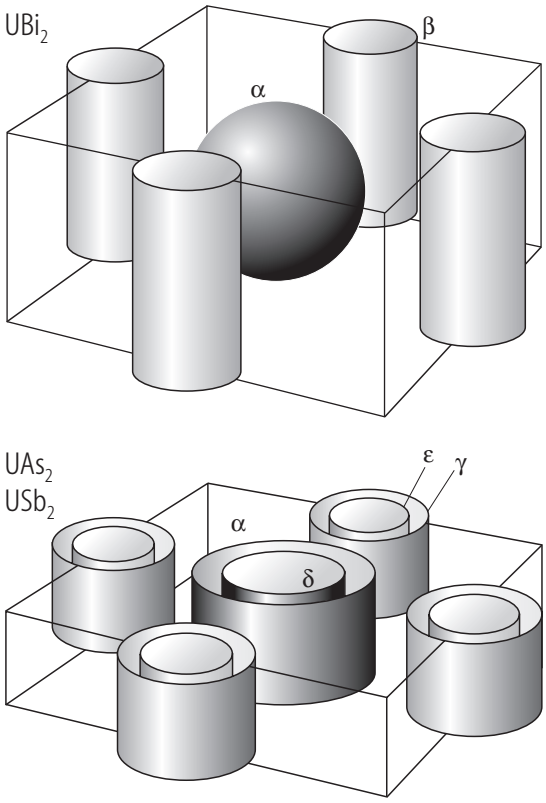

Fig. 321. UX_2, X = As, Sb and Bi. Schematic magnetic Brillouin zone and the Fermi surfaces derived in the de Haas – van Alphen studies [00AWMW]. The Fermi surface in UBi_2 consists of a cylindrical hole sheet β that is very close to the Brillouin zone boundary and a spherical electron sheet α. The calculated electronic specific heat coefficient $\gamma_s(0)$ is 18 mJ/mol K^2 being in a very good agreement with the experimental data of 20 mJ/mol K^2 (see Fig. 364). In UAs_2 and USb_2 all the Fermi surfaces are cylindrical. With the assumption that branches α and δ contain electrons and branches γ and ε contain holes, an equal number of electrons and holes is achieved, thus accounting for a compensated metallic character of these compounds. The estimated electronic specific heat coefficient $\gamma_s(0)$ = 10 and 21 mJ/mol K^2 for UAs_2 and USb_2, respectively, is consistent with the experimental results of 12 and 26 mJ/mol K^2, respectively (see Figs. 314 and 347).

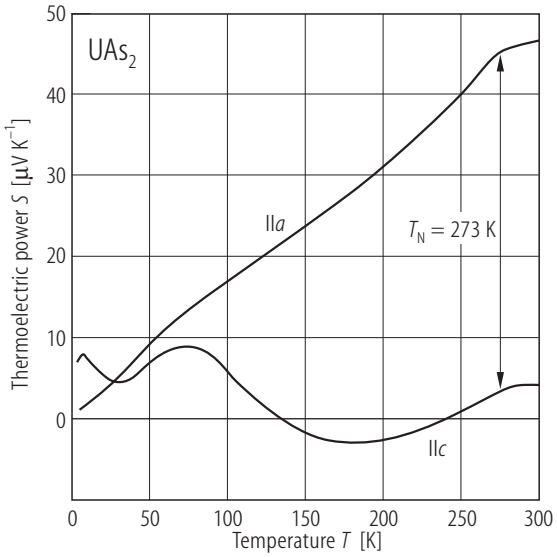

Fig. 322. UAs_2, sc. Thermoelectric power, *S*, vs. temperature, *T*, measured along the *a*- and *c*-axes [02HWWK]. The arrows mark the antiferromagnetic phase transition. Note two-peak structure at low temperatures in *S*(*T*) taken along the *c*-axis.

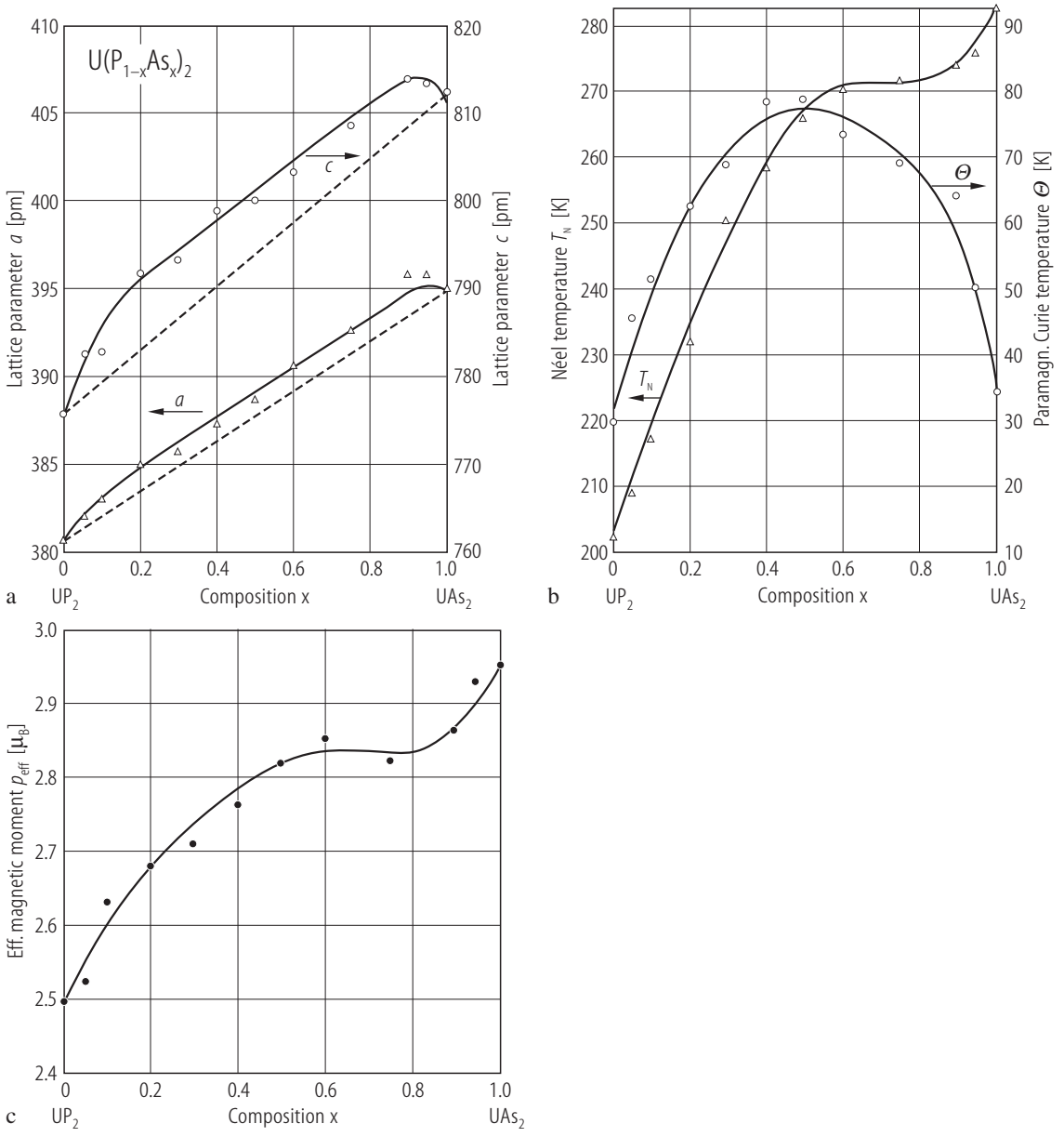

Fig. 323. $U(P_{1-x}As_x)_2$. **(a)** Tetragonal lattice parameters, *a* (triangles; left-hand scale) and *c* (circles; right-hand scale), vs. As content, x [68TM]. UP_2 exhibits a complete miscibility with UAs_2 with positive deviation of both lattice parameters from Vegard's law (marked by the dashed lines). **(b)** Néel temperature, T_N (triangles; left-hand scale), and paramagnetic Curie temperature, Θ (circles; right-hand scale) vs. As content, x [68TM]. **(c)** Effective magnetic moment, p_{eff}, vs. As content, x [68TM]. Note that T_N and p_{eff} gradually rise with x up to about 50 mol% UAs_2 and then hardly change, while Θ shows a maximum at about 50 mol% UAs_2.

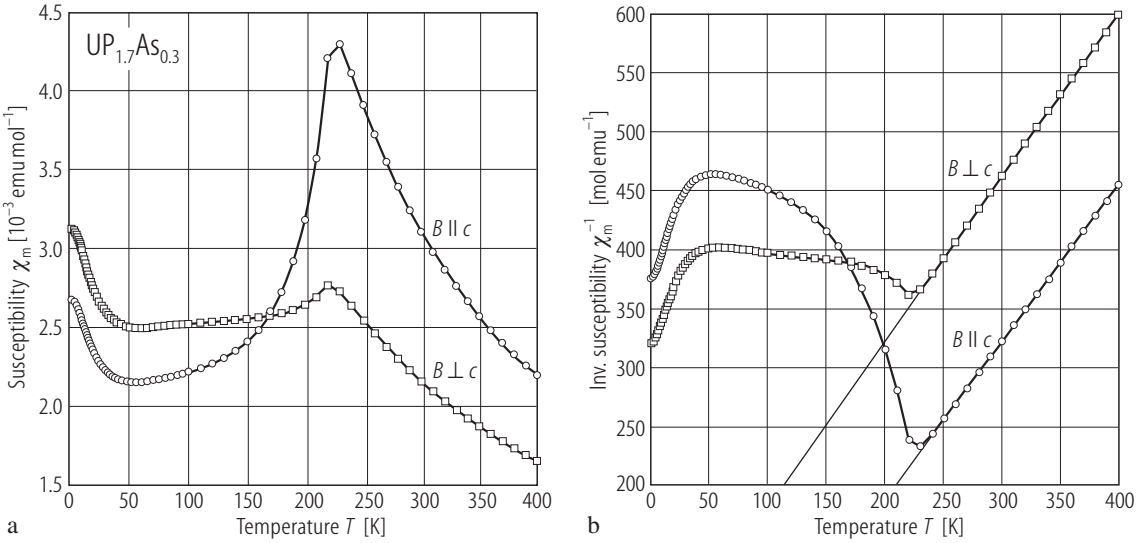

Fig. 324. $UP_{1.7}As_{0.3}$, sc. **(a)** Molar magnetic susceptibility, χ_m, vs. temperature, T, in the range 1.7…400 K, measured along the c-axis (open circles) and in the (ab)-plane (open squares) [02TSKP]. The compound orders antiferromagnetically at T_N = 223 K. The tails in $\chi_m(T)$ at low temperatures have unknown origin. **(b)** Inverse molar magnetic susceptibility, χ_m^{-1}, vs. T, measured as in panel **(a)** [02TSKP]. The solid lines are Curie Weiss fits with the parameters given in Table F.

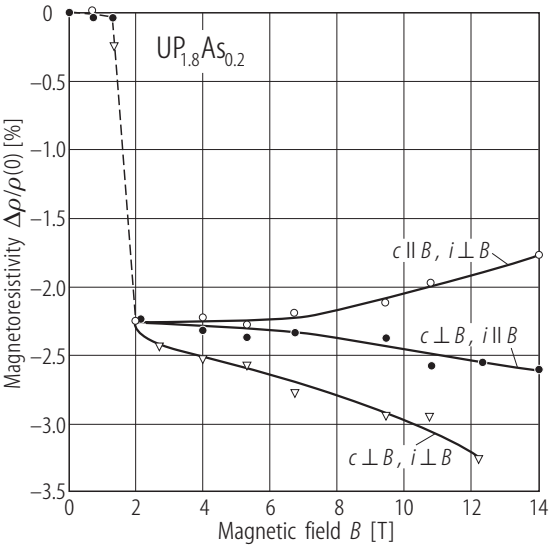

Fig. 325. $UP_{1.8}As_{0.2}$, sc. Magnetoresistivity, $\Delta\rho/\rho(0)$, vs. magnetic field, B, measured at T = 4.2 K up to 14 T with i ∥ a-axis (hard magnetization direction) in magnetic field B ∥ c-axis (open circles), B ∥ b-axis (open triangles) and B ∥ a-axis (filled circles) [98HCPF]. Note a step-like change in $\Delta\rho/\rho(0)$ between 1.6 and 2 T. The magnitude of this jump and the critical field do not depend on the field direction. Thus it cannot be a metamagnetic transition but may rather result from the formation of an isotropic magnetic impurity state in strongly anisotropic UP_2 matrix when a small part of P atoms are replaced by As atoms.

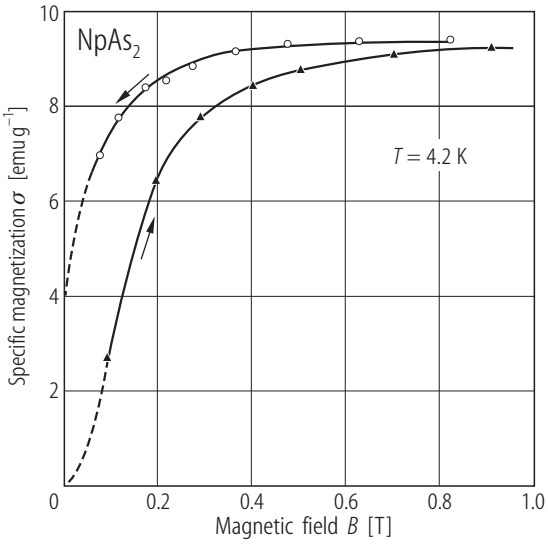

Fig. 326. $NpAs_2$. Specific magnetization, σ, vs. magnetic field, B, taken at T = 4.2 K with increasing (full symbols) and decreasing (open symbols) magnetic field [82BFDW]. The saturation magnetic moment p_s is 0.66 μ_B/Np atom, which is almost half the value found from neutron diffraction experiments (see Fig. 332). The remanent magnetization σ_r is about 4 emu/g and the coercive field $\mu_o H_c$ is 0.06 T (not shown)

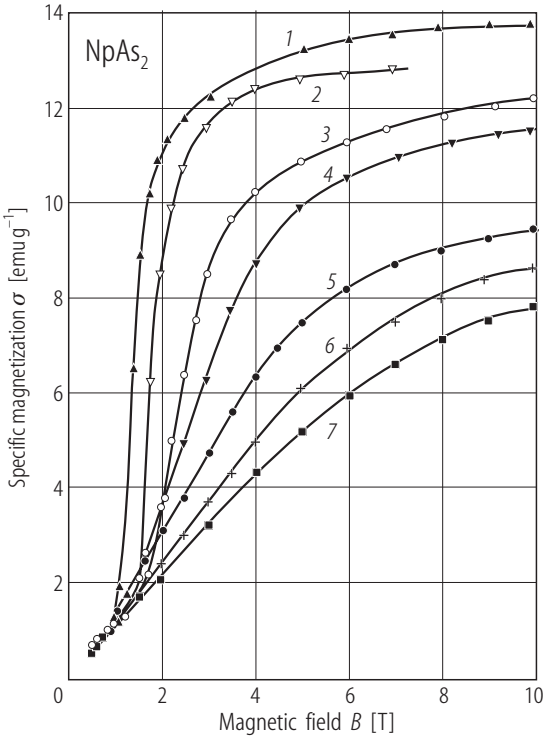

Fig. 327. $NpAs_2$. Specific magnetization, σ, vs. magnetic field, B, taken at various temperatures in the range $32 < T < 60$ K and with increasing magnetic field [82BFDW]. *1* - 32.5 K; *2* - 36 K; *3* - 42.5 K; *4* - 48 K; *5* - 51 K; *6* - 54 K; *7* - 60 K. Between $T_N = 52$ K and $T_t = 18$ K the compound is antiferromagnetic. Note the occurrence of a metamagnetic-like transition in a relatively weak magnetic field of about 1.5 T.

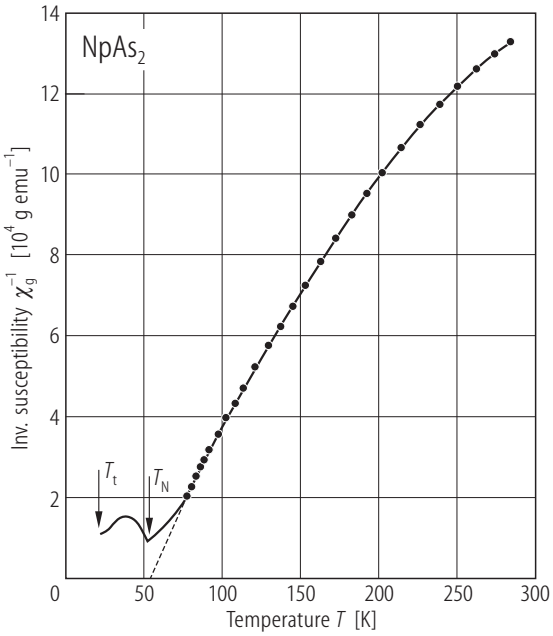

Fig. 328. $NpAs_2$. Inverse mass magnetic susceptibility, χ_g^{-1}, vs. temperature, T, measured in a field of 0.3135 T [82BFDW]. The dashed line is a modified Curie-Weiss fit with the parameters given in Table F. The compound orders antiferromagnetically at $T_N = 52$ K and then undergoes a transition into a ferromagnetic state at $T_t = 18$ K.

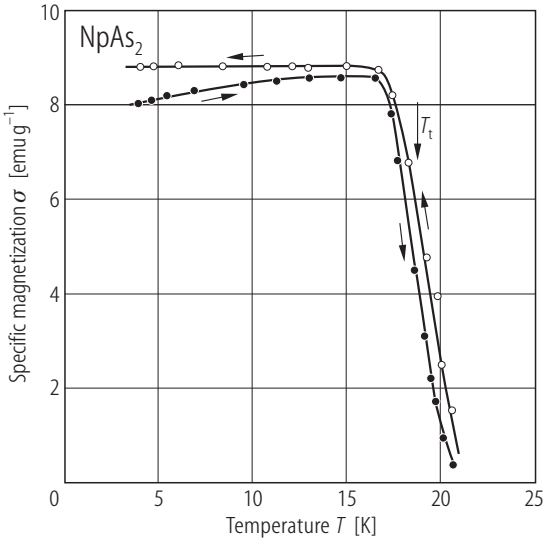

Fig. 329. $NpAs_2$. Specific magnetization, σ, vs. temperature, T, below 20 K, measured in a field of 0.3135 T with increasing (full symbols) and decreasing (open symbols) temperature [82BFDW]. Note small irreversibility in $\sigma(T)$ characteristic of magnetic anisotropy connected with the presence of narrow domain walls. The transition at T_t is of the first order type.

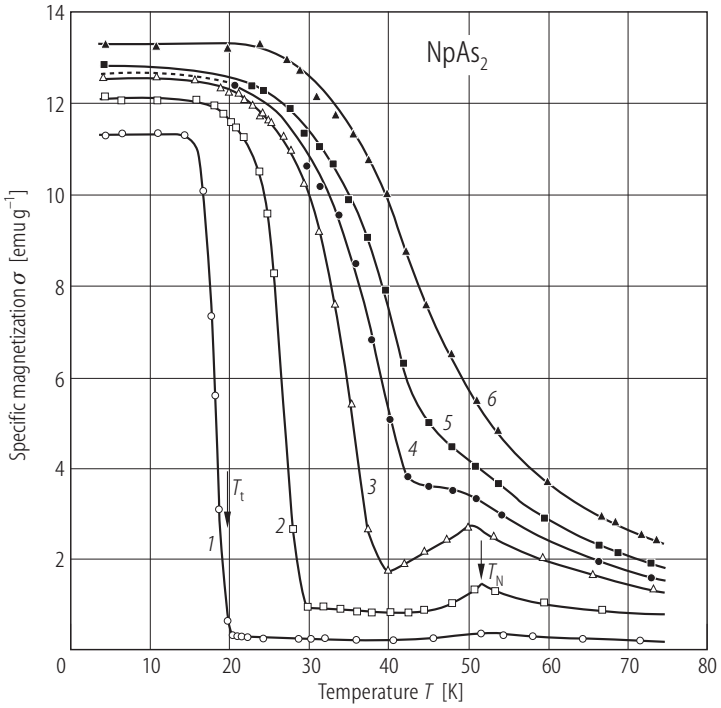

Fig. 330. $NpAs_2$. Specific magnetization, σ, vs. temperature, T, below 75 K, measured in various fields in the range $0 < B < 3$ T [82BFDW]. *1* - 0.229 T; *2* - 0.916 T; *3* - 1.707 T; *4* - 2.1 T; *5* - 2.475 T; *6* - 3.0 T. Note that when an applied field increases, the first order transition (see Fig. 332) at T_t to ferromagnetic state shifts towards the Néel temperature and the antiferromagnetic phase disappears for $B = 3$ T.

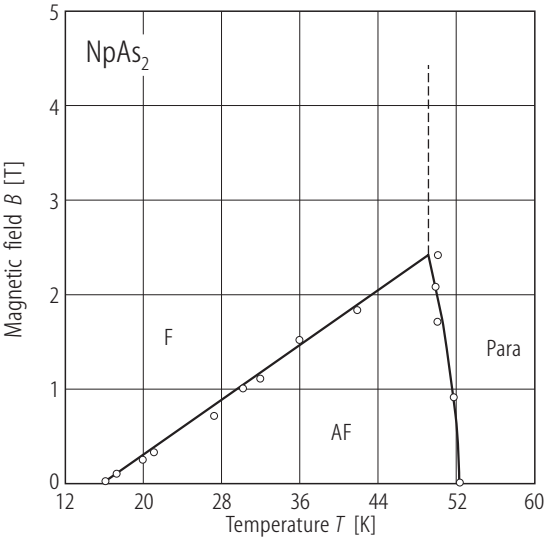

Fig. 331. $NpAs_2$. Magnetic phase diagram, as deduced from magnetization measurements [82BFDW]. In weak magnetic fields the compound is ferromagnetic up to $T_t = 18$ K, antiferromagnetic for $T_t < T < T_N = 52$ K, and then paramagnetic. The transitions at T_t and T_N are first order ones (see Fig. 332). With increasing field the antiferromagnetic region shrinks and entirely disappears in fields $B > 2.5$ T. This finding is however in contradiction to the electrical resistivity data (compare Fig. 339).

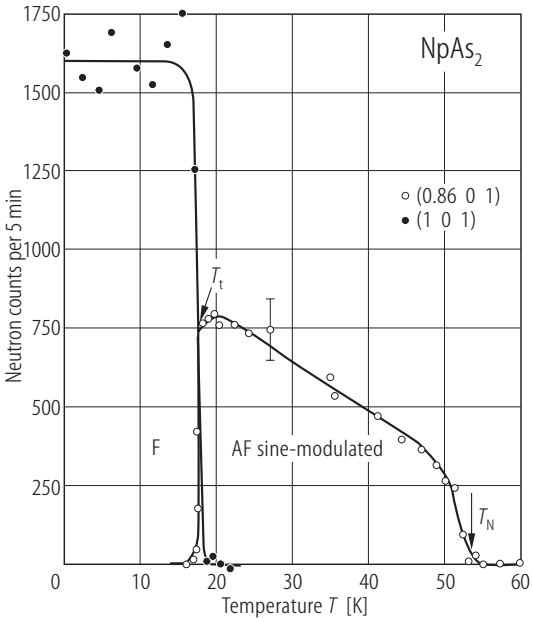

Fig. 332. $NpAs_2$, sc. Neutron diffraction intensity of a magnetic Bragg peak (1 0 1) (full circles) and an incommensurate peak (0.86 0 1) (open circles) vs. temperature, T, below 60 K [82RBQB]. A first-order phase transition from the low-temperature ferromagnetic state to the high-temperature sine modulated antiferromagnetic state occurs at $T_t = 18.5$ K (see also Fig. 331). At all temperatures the Np magnetic moments, p_{Np}, are oriented along the tetragonal c-axis. The ordered moment taken at 5 K amounts to 1.45(1) μ_B. The magnetic structure above T_t is described in Fig. 333.

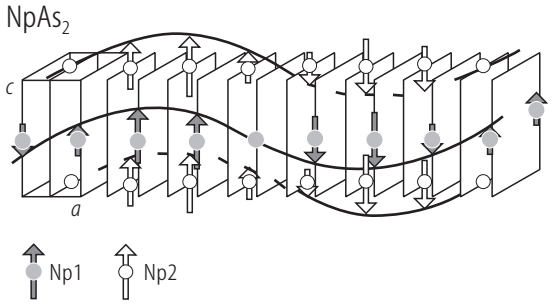

Fig. 333. $NpAs_2$. Magnetic structure formed in the antiferromagnetic state between T_t = 18.5 K and T_N = 52 K [82RBQB]. The Np magnetic moments are aligned along the *c*-axis and form a sine-wave modulated structure propagating along the [100] direction and extending over seven Np sites. The propagation vector $\boldsymbol{k}$ is temperature independent from T_N down to T_t and amounts $\boldsymbol{k}$ = (0.141,0,0), i.e. it is incommensurate with the lattice.

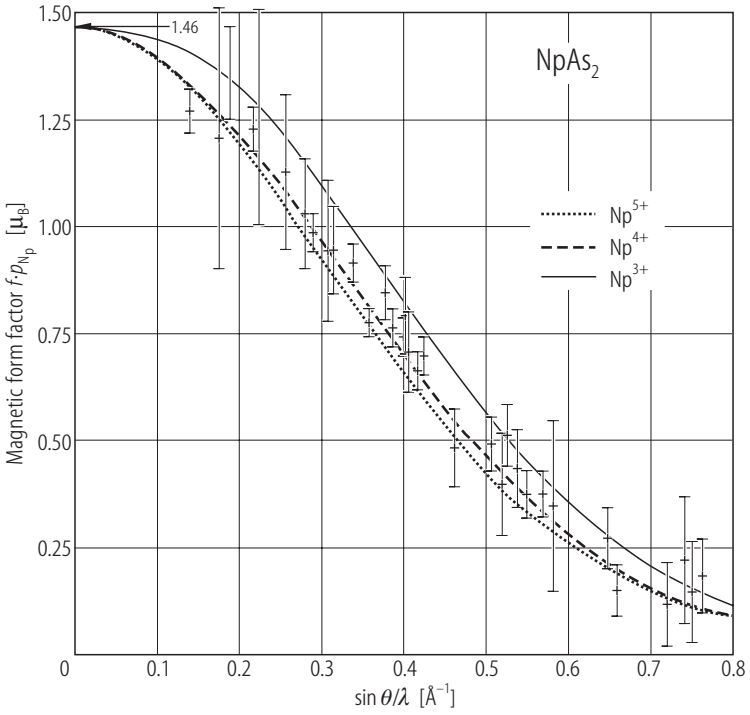

Fig. 334. $NpAs_2$, sc. Magnetic form factor of neptunium atom determined via polarized neutron diffraction at T = 4.2 K (ferromagnetic state) [82DMBF]. For comparison there are shown the theoretical form factors for Np^{3+}(solid line), Np^{4+} (dashed line) and Np^{5+} (dotted line) free ions. Note that the best agreement is obtained for both the 4+ and 5+ charges, however a Np^{5+} charge state is ruled out due to the value of the isomer shift (see Introduction).

For Figs. 335, 336 see next pages

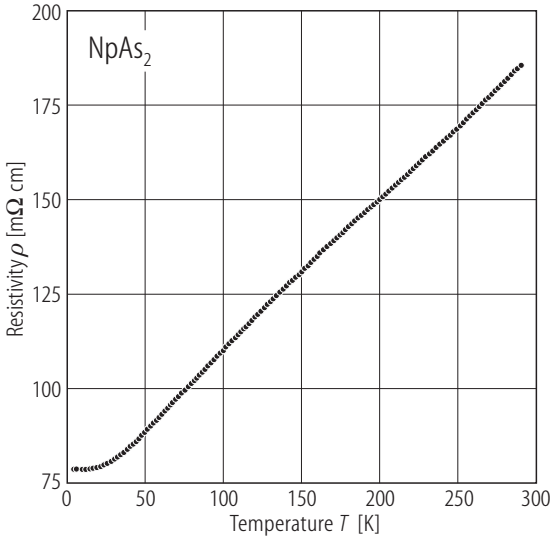

Fig. 337. $NpAs_2$. Electrical resistivity, ρ, vs. temperature, T, measured on cold pressed powder sample [81BDS]. Note that no anomalies are seen at the magnetic phase transitions at T_N = 48 K and T_t = 17.8 K. A simple metallic character of $\rho(T)$ contrasts with the single crystal resistivity data (compare Fig. 338).

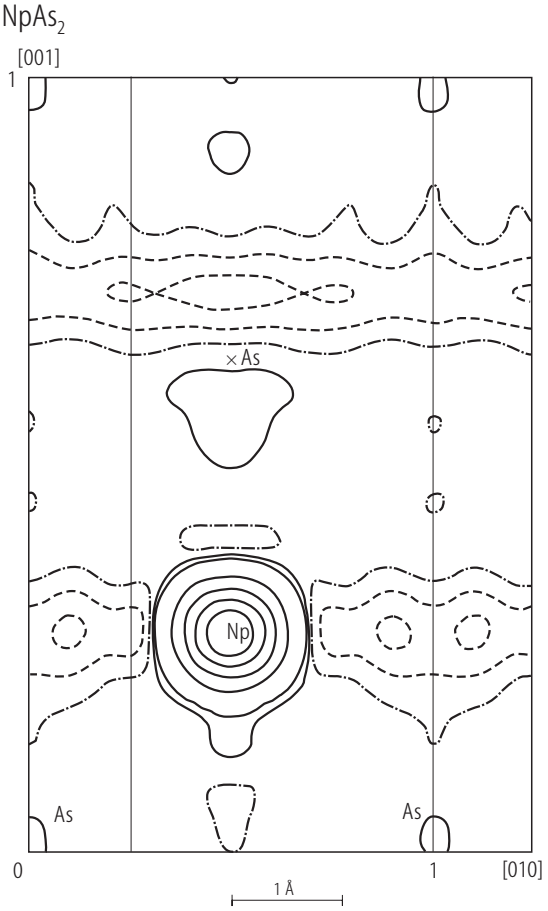

Fig. 335. $NpAs_2$, sc. Magnetization density map for a section perpendicular to the [100] axis [82DMBF]. The lines stand for contours of the same density (values not given). Note a well localized character of the 5f electrons around Np atoms.

Fig. 336. $NpAs_2$. **(a)** ^{237}Np Mössbauer spectra at various temperatures from 4.2 to 60 K taken against a ^{241}Am metal source [82BCAK]. The solid lines are least-squares fits. Above 52 K the spectra show a single resonance line with unresolved quadrupole coupling, which corresponds to a paramagnetic state. Below 18 K the spectra correspond to a single site combined magnetic and quadrupolar hyperfine pattern, compatible with a ferromagnetic spin structure (see Fig. 331). At T = 4.2 K the relevant hyperfine parameters are as follows: B_{hf} = 288 T, e^2qQ/h = 1100 MHz, IS = 3.0 mm/s (relative to $NpAl_2$), Γ = 4.5 mm/s. The isomer shift indicates the 4+ charge state for Np, and the hyperfine field implies a magnetic moment of 1.5 μ_B/Np. Above 18 K the spectra are more complex indicating a sinusoidally modulated antiferromagnetic structure with a period over roughly seven Np sites (see Fig. 333). The spectra can be separated into five overlayed hyperfine patterns with different spectral parameters (for the details refer to the original paper). Both magnetic phase transitions have a first-order character on an account of the occurrence of hysteresis effect around T_t and T_N. **(b)** Moment modulation over seven Np nuclei, which assigns at 25 K the five different hyperfine fields B_{hf} indicated by the arrows [82BCAK].

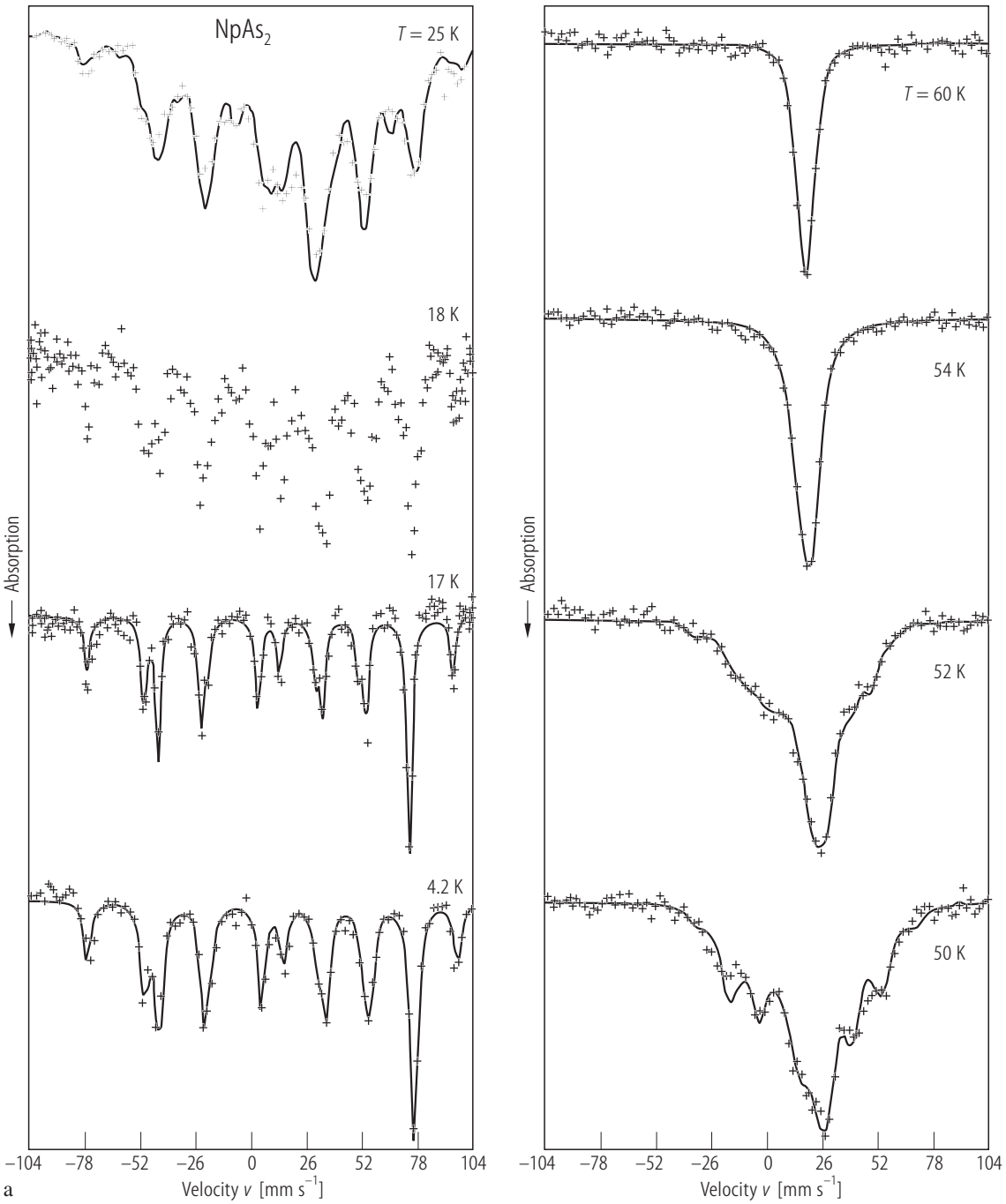

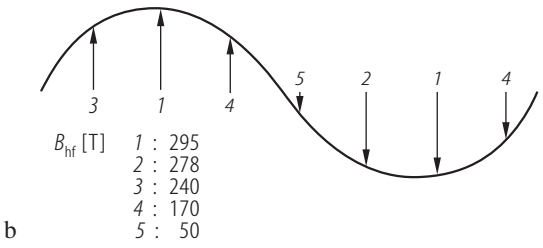

Fig. 336. For caption see previous page

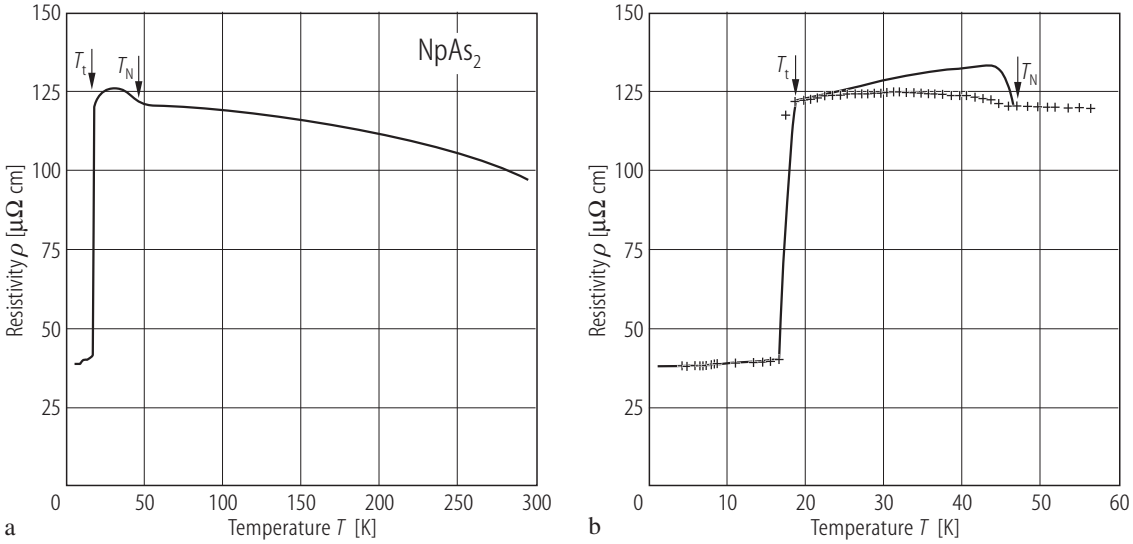

Fig. 338. $NpAs_2$, sc. **(a)** Electrical resistivity, ρ, vs. temperature, T, measured with the current flowing in the (*ab*)-plane of the tetragonal crystal structure [85TBFC]. The antiferromagnetic phase transition manifests itself as an anomaly in the temperature derivative of the resistivity at T_N = 48(1) K (not shown). The antiferro-ferromagnetic transition is seen as a sudden drop in $\rho(T)$ at T_t = 17.8(1) K. Both transitions have a first-order character (see also the magnetic data in Fig. 330). **(b)** Low temperature behaviour of $\rho(T)$ [85TBFC]. The solid line is a theoretical curve obtained in the framework of the Elliott and Wedgwood's theory (for the details refer to the original paper). Below 17 K the resistivity exhibits a T^2 behaviour (see Fig. 339), characteristic of scattering of conduction electrons on ferromagnetic spin-wave excitations.

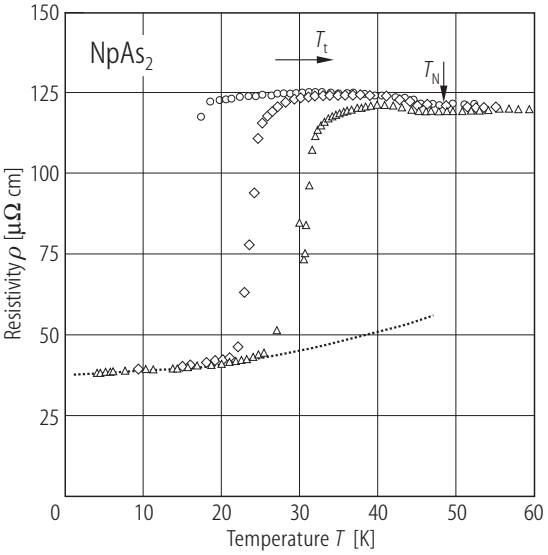

Fig. 339. $NpAs_2$, sc. Electrical resistivity, ρ, vs. temperature, T, measured with the current flowing in the (*ab*)-plane of the tetragonal crystal structure, in a magnetic field applied along the current [85TBFC]. Circles: zero field; diamonds: 5 T; triangles: 10 T. Note that contrary to magnetic study (compare Fig. 331) the AF phase is not destroyed even by a field of 10 T. With increasing field the para-antiferromagnetic transition T_N hardly shifts to lower temperatures while the antiferro-ferromagnetic transition T_t considerably shifts to higher temperatures, however the shape of $\rho(T)$ in the two ordered regions is only slightly affected by magnetic field. The dotted curve marks a T^2 dependence.

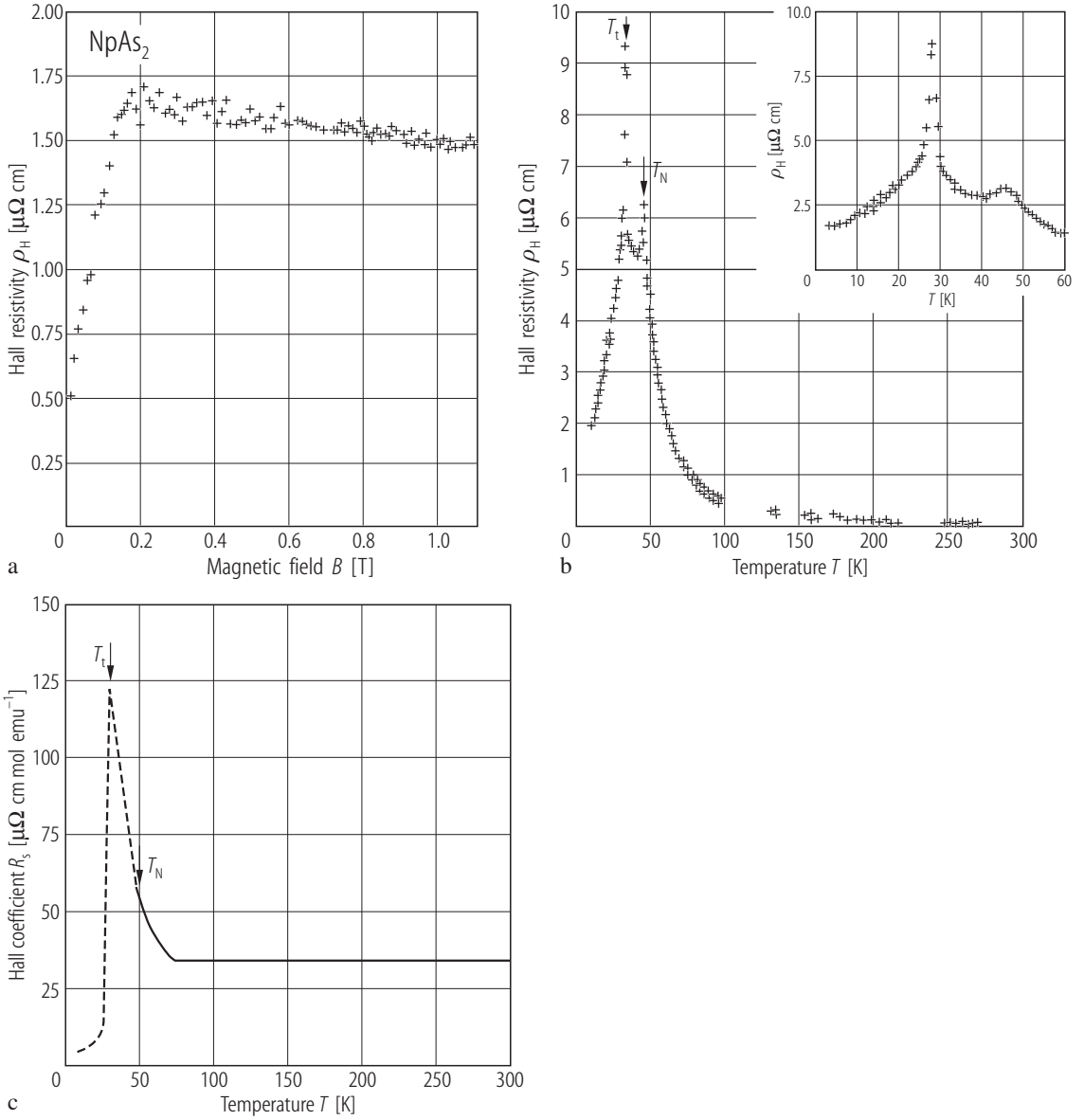

Fig. 340. $NpAs_2$, sc. **(a)** Hall resistivity, ρ_H, vs. magnetic field, B, applied along the [001] axis measured at $T = 4.2$ K, i.e. in the ferromagnetic state [86TBCF]. The Hall resistivity analyzed according to the formula $\rho_H = R_o B + R_s M$ where M is the magnetization, yields the normal Hall coefficient R_o = –0.26 μVcm/K, which corresponds in a one-band model to the electron concentration n_H of 2.84…10^{27} m^{-3} i.e. 0.22 el/f.u. **(b)** Hall resistivity, ρ_H, vs. temperature, T, in the range 4.2…300 K, measured in a magnetic field of 0.67 T applied along the [001] axis [86TBCF]. Inset: $\rho_H(T)$ in the range 4.2…60 K taken in a field of 1.07 T applied along the [001] axis. The phase transitions at T_N = 52 K and T_t = 18 K manifest themselves as sharp peaks in $\rho_H(T)$. Note that an increase in the magnetic field strength suppresses the peak at T_N, leaving almost unaffected that one at T_t. In the paramagnetic region the Hall resistivity decreases according to the formula $\rho_H = R_o B + R_s \chi B$. For the susceptibility taken from [82BFDW] one finds R_o = –0.11 μVcm/K, which yields the electron concentration n_H = 0.44 el/f.u. Note that this value is twice than derived in the ferromagnetic region (compare panel **(a)**). **(c)** Anomalous Hall coefficient, R_s, vs. temperature, T, estimated from the data shown in panel **(b)** [86TBCF]. Above 75 K R_s is temperature independent. At lower temperatures, down to T_N, R_s increases due to magnetic short-range interactions. In the antiferromagnetic region (dashed curve) R_s further rises with decreasing temperature in an almost linear manner. At T_t there is a rapid drop in $R_s(T)$ and in the ferromagnetic state R_s is proportional to the resistivity (see Fig. 338).

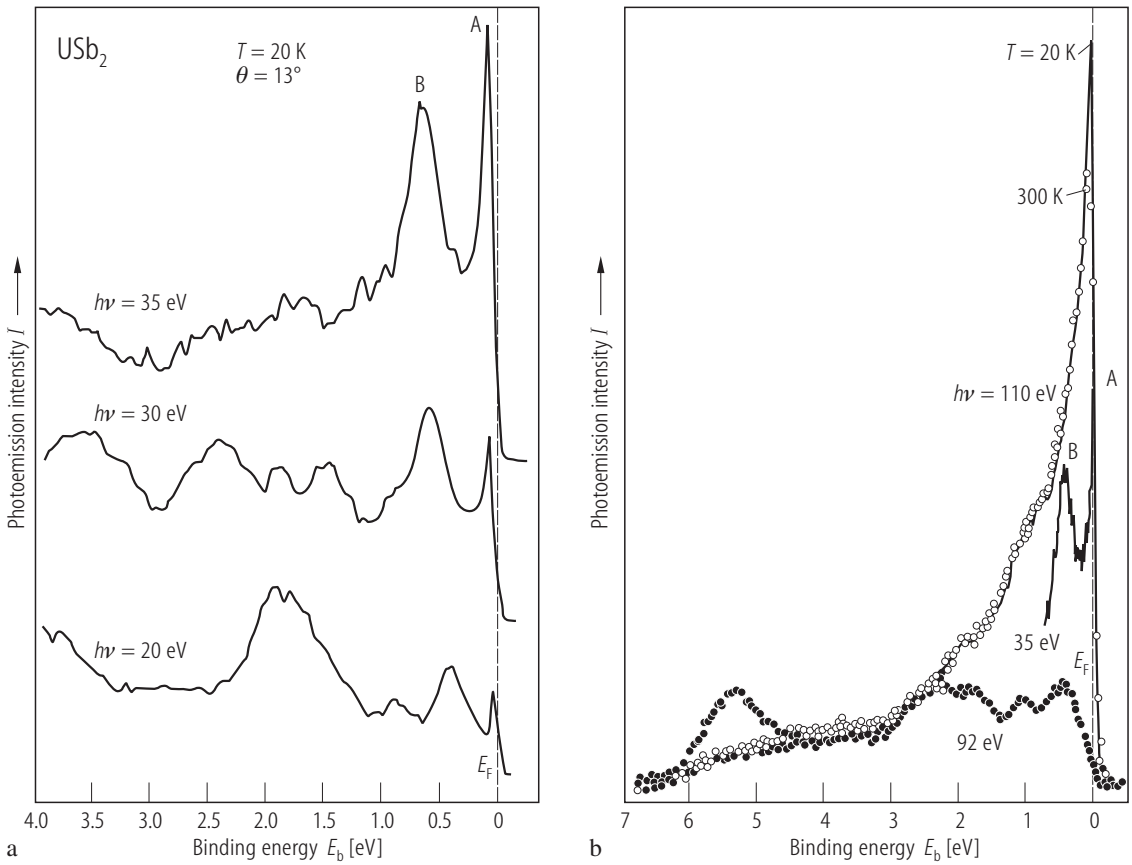

Fig. 341. USb_2, sc. **(a)** Angle-resolved photoemission spectra taken at constant analyser angle 13º from the normal to the (001) surface and at T = 20 K with photon energies $h\nu$ = 20, 30 and 35 eV [97AJAM, 98AJCM]. The resolution ΔE < 40 meV. A rapid growth of the intensity of features A and B with rising $h\nu$ indicates their f-character. The sharp peak A increases slightly more quickly than the broad peak B, probably because the latter feature acquires also some 6d character, as it disperses away from E_F with increasing $h\nu$. The other features at higher binding energies are primarily 6p-6d - derived dispersive peaks. **(b)** Normal emission spectra at resonance (110 eV) and antiresonance (92 eV) at T = 20 K (solid line) and 300 K (open circles) [97AJAM]. For comparison an off-normal spectrum (about 10º from Γ towards X) measured at 35 eV and 20 K is shown to emphasize the narrow 5f feature A. Note that in the resonant spectrum only the intensity within about 0.6 eV of E_F results from f states. A major source of triangular shape of this spectrum is the 6d resonance. The thermal behaviour is conventional and completely accounted for by 100 meV of phonon broadening and Fermi function effects.

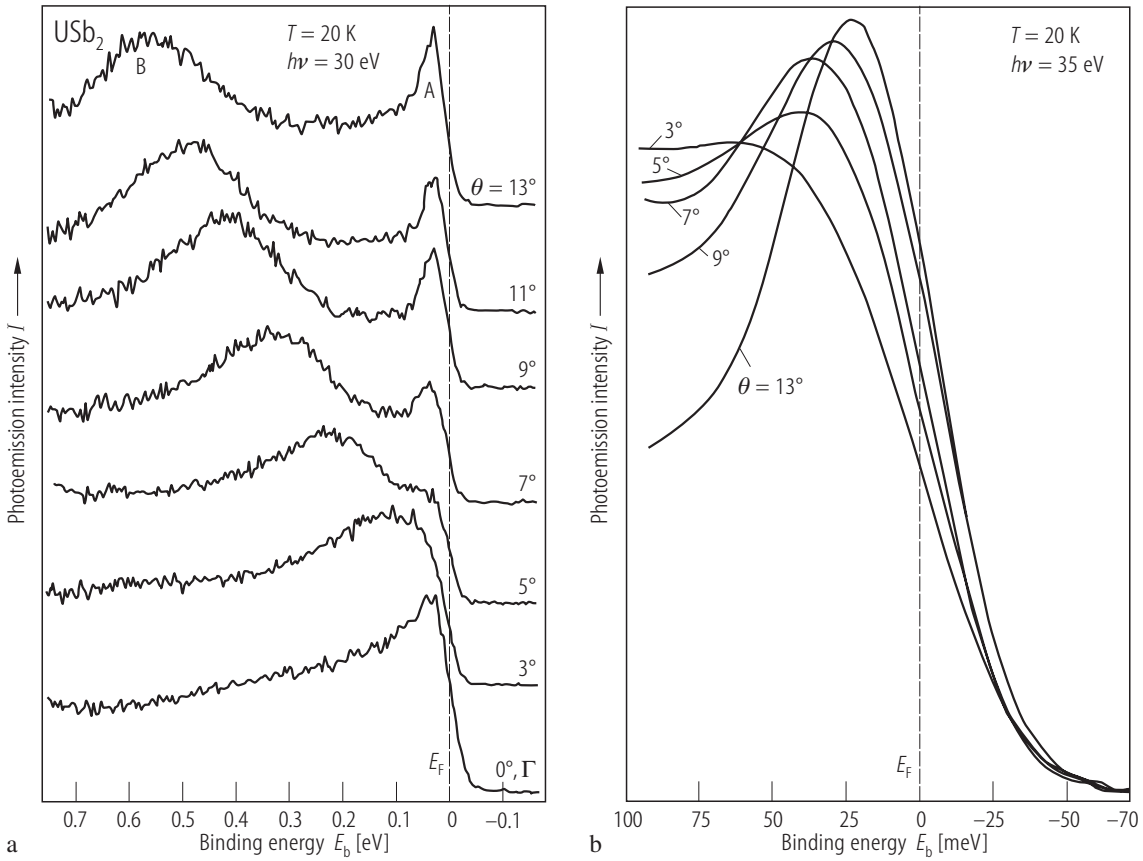

Fig. 342. USb_2, sc. **(a)** High-resolution angle-resolved photoemission spectra within 800 meV of E_F at $h\nu = 30$ eV and $T = 20$ K taken along the Γ - X direction in the zone, at analyser angles specified in the figure [97AJAM]. Dispersion of peak B is clearly evident (from –600 meV through E_F at the Γ point). In contrast, peak A is nearly dispersionless but exhibits an intense amplitude modulation at Γ (0°). **(b)** Expanded view of ARPES spectra taken as in panel **(a)** at $T = 20$ K but with $h\nu = 35$ eV [97AJAM, 97AJAT]. Amplitude normalization is arbitrary to facilitate viewing small dispersion of peak A (about 39 meV). From the flatness and 5f origin of this band there is concluded that strong electron correlations and the ordered magnetic moment are confined to band A and energies very close to the Fermi level. The data strongly support a temperature-invariant band nature of 5f-states [97AJAT].

Fig. 343. USb_2, sc. ARPES spectra measured at $T = 25$ K with the HeIα resonance line ($h\nu = 21.218$ eV) along the Γ–M direction, as shown in the top panel [02KIST]. In a sketch depicting the 2D projected BZ there are indicated the α, β, γ and ε sheets of FS deduced from dHvA measurements (see [99AWMW] and [00AWMW]). **(a)** Ultrahigh resolution ARPES spectra showing two prominent dispersionless peaks A and B near E_F, assigned to the 5f states (see panel **(b)**), which correspond to single but slightly dispersive peak A reported in [97AJAM], as well as peak C, which corresponds to peak B found in [97AJAM] (compare Fig. 342). **(b)** Ultrahigh resolution ARPES spectra in the vicinity of the Fermi level, showing the dispersion of the U 5f peaks. Note the almost flat 5f bands around the M point and their sudden dispersive character towards E_F around 40% of Γ–M symmetry line, where band C also approaches E_F. The narrow U 5f bands hybridized with highly dispersive Sb-sp bands make moderately heavy FS with $m_{eff} = 5.1\ m_0$. Compare these results with the dHvA data shown in Fig. 355.

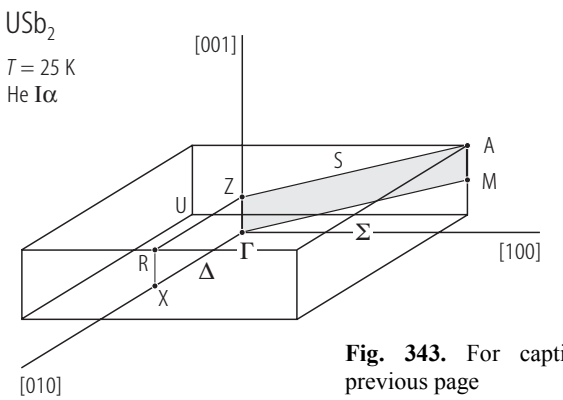

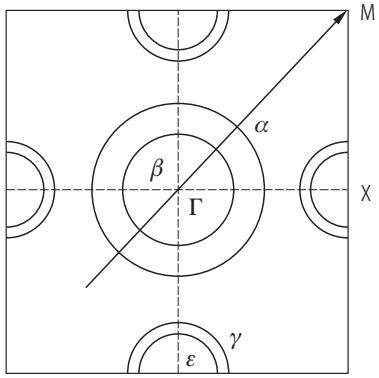

Fig. 343. For caption see previous page

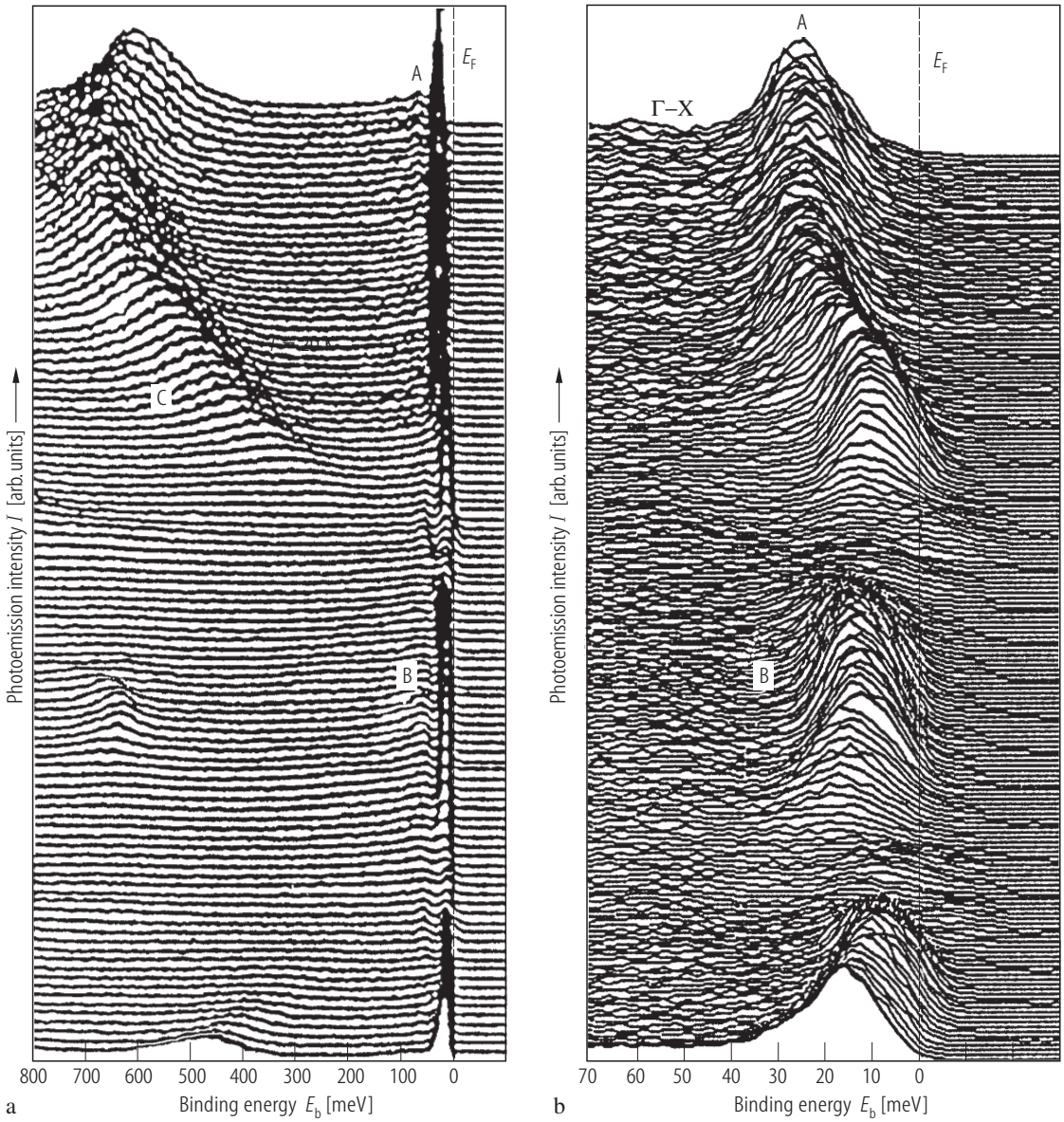

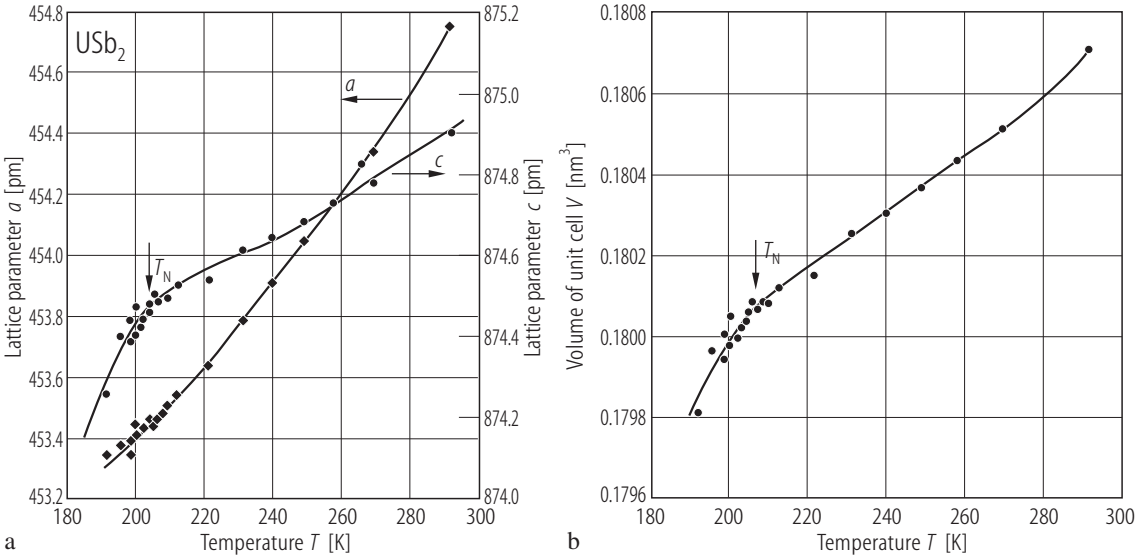

Fig. 344. USb_2, sc. **(a)** Tetragonal lattice parameters, a and c, vs. temperature T, in the range 190…300 K [77LPKM]. Note a kink in the c parameter at the Néel temperature T_N = 203 K. **(b)** Unit cell volume, V, vs. temperature T [77LPKM].

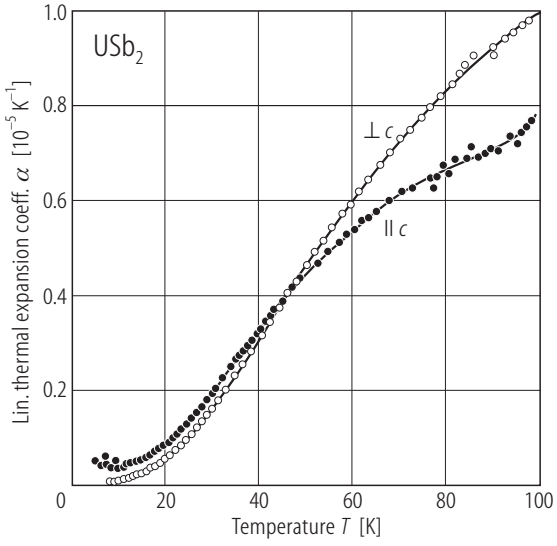

Fig. 345. USb_2, sc. Thermal expansion coefficient, α, vs. temperature, T, below 100 K, measured along the c-axis (full circles) and in the (ab)-plane (open circles) [92HMWF]. The solid lines are guides for the eye. Note that the anisotropy in $\alpha(T)$ is rather small, in contrast to strongly anisotropic behavior of the resistivity (see Fig. 348).

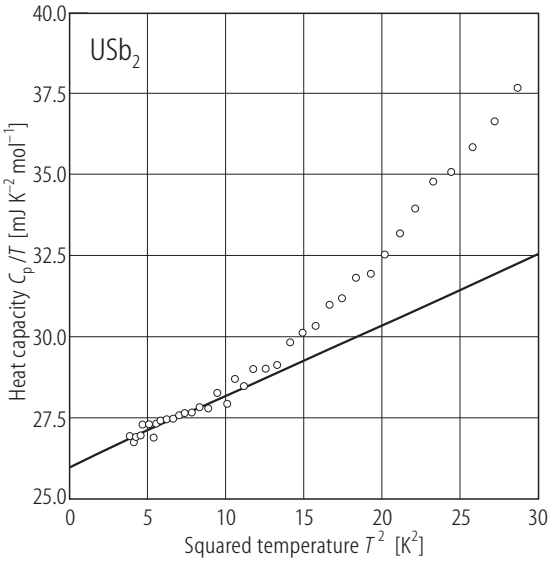

Fig. 347. USb_2. Heat capacity over temperature, C_p/T, vs. squared temperature, T^2, in the range 2…5.3 K [99AWMW]. The solid line is a fit to the expression $C/T = \gamma(0) + \beta T^2$ yielding the electronic specific heat coefficient $\gamma(0)$ = 26 mJ/mol K^2.

For Fig. 346 see next page

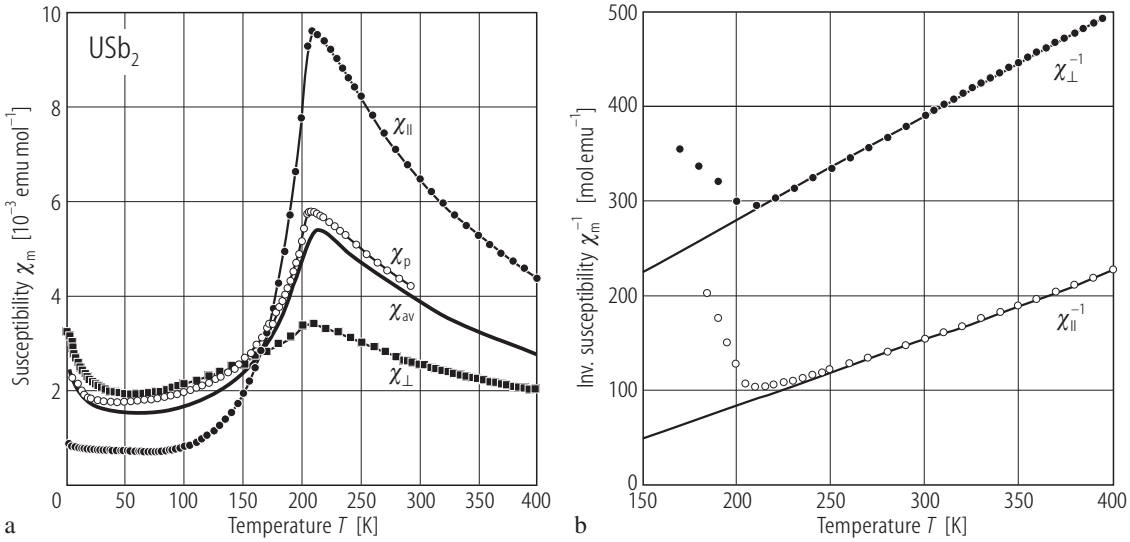

Fig. 346. USb_2, sc. **(a)** Molar magnetic susceptibility, χ_m, vs. temperature, T, in the range 1.7…400 K, measured along the c-axis (full circles) and in the (ab)-plane (full squares) [02TBSP]. The thick solid line represents an average molar susceptibility $\chi_{av} = 1/3\ (2\chi_\perp + \chi_\parallel)$. For comparison the susceptibility measured on a polycrystalline sample is also shown (open circles). The compound orders antiferromagnetically at T_N = 203 K. **(b)** Inverse molar magnetic susceptibility, χ_m^{-1}, vs. T, measured as in panel **(a)** [02TBSP]. The solid lines are Curie Weiss fits with the parameters given in Table F.

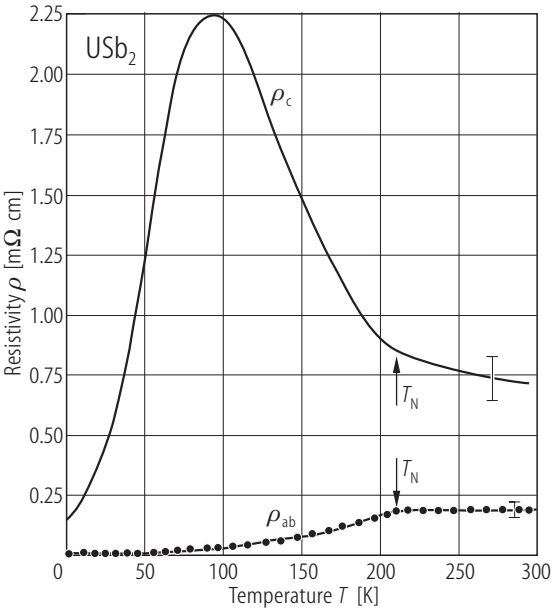

Fig. 348. USb_2, sc. Electrical resistivity, ρ, vs. temperature, T, measured with the current flowing along the c-axis (ρ_c) and in the (ab)-plane (ρ_{ab}) [92HMWF]. The full circles correspond to the data taken from [72HK]. At T_N = 203 K there are pronounced kinks in both ρ_c and ρ_{ab} yielding cusps in the temperature derivative of the resistivity having opposite signs. Below T_N, $\rho_c(T)$ shows a large maximum characteristic of antiferromagnetic materials. From T_N down to the lowest temperatures $\rho_c(T)$ follows a $T^{5/2}$ relation (see also Fig. 318). Note a decrease in ρ_c with increasing temperature in the paramagnetic region resembling Kondo-like effect. The ratio ρ_c/ρ_{ab} increases from 3.5 at ambient temperatures up to a maximum value of 162 at 50 K (compare Fig. 349b).

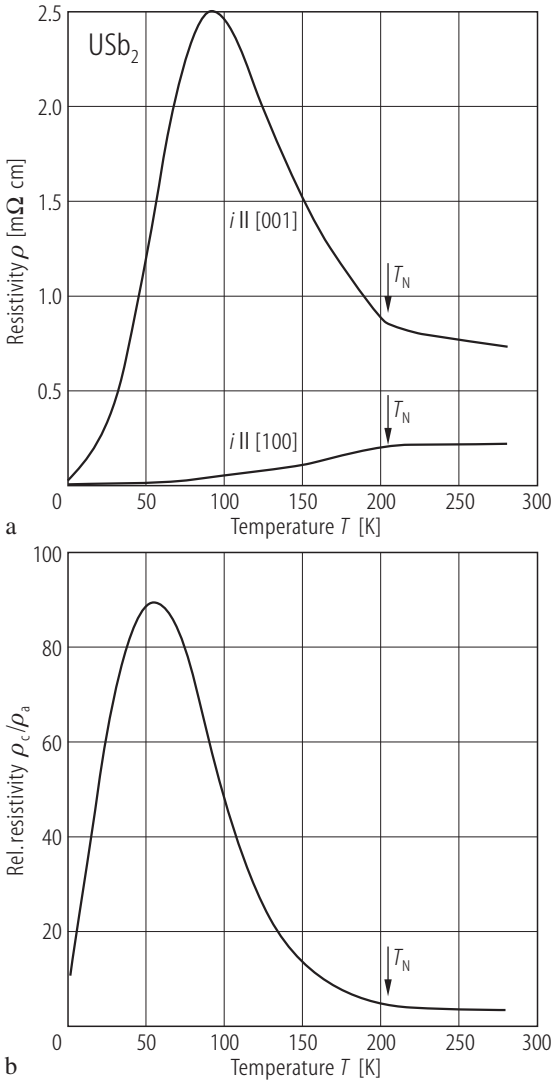

Fig. 349. USb_2, sc. **(a)** Electrical resistivity, ρ, vs. temperature, T, down to 0.1 K with the current flowing along the [100] (lower curve) and [001] (upper curve) directions [00AWMW]. RRR along [100] is 81 and ρ_0 is 2.9 μΩcm. The arrows mark the antiferromagnetic phase transition at T_N = 203 K. Note a large hump in $\rho_c(T)$ below T_N indicating a reconstruction of the Fermi surface due to a small flattened magnetic Brillouin zone corresponding to the magnetic unit cell doubled along the [001] axis with respect to the crystallographic unit cell (see Fig. 283). **(b)** The anisotropy ratio, ρ_c/ρ_a, vs. T [00AWMW]. Note that the resistivity anisotropy is rather small (maximum ρ_c/ρ_a of about 90 at 60 K) in comparison to the behaviour of UBi_2 (ρ_c/ρ_a = 820 at 80 K; see Fig. 365).

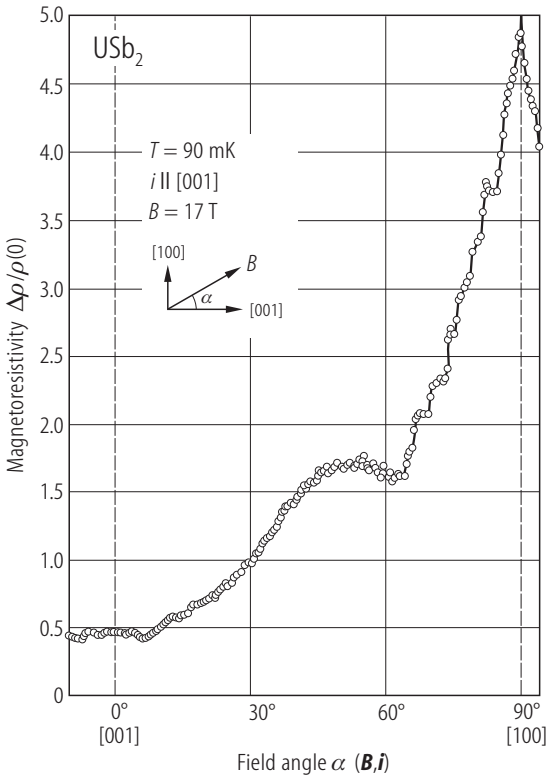

Fig. 351. USb_2, sc. Magnetoresistivity, $\Delta\rho/\rho(0)$, vs. angle $\alpha(\boldsymbol{B},\boldsymbol{i})$ between magnetic field and electrical current, measured at T = 90 mK in the magnetic field of 17 T with the current flowing along the [001] axis [00AWMW]. Note a large anisotropy of $\Delta\rho/\rho(0)$ yielding a sharp peak at [100].

For Fig. 350 see next page

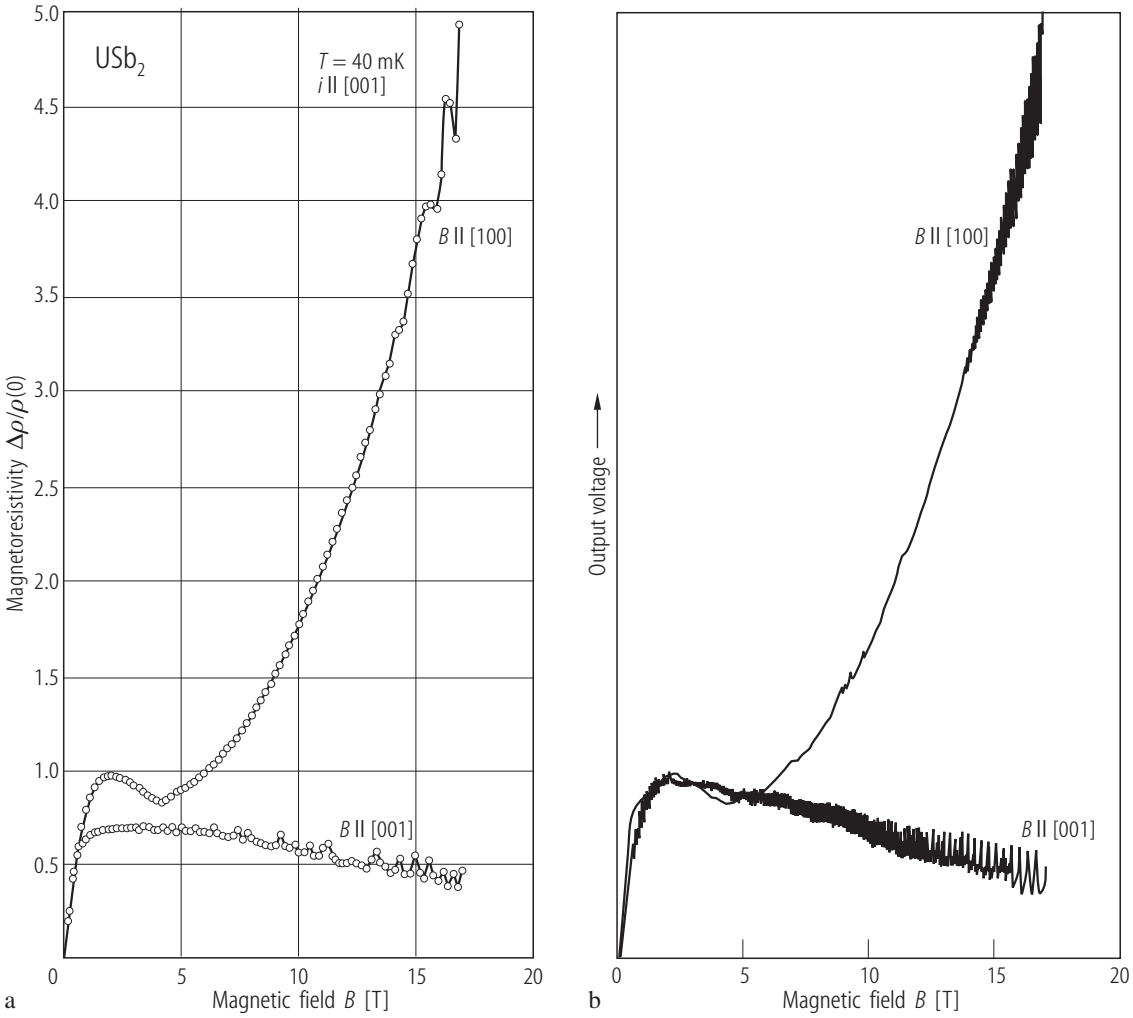

Fig. 350. USb_2, sc. Magnetoresistivity, $\Delta\rho/\rho(0)$, vs. magnetic field, B, measured at T = 40 mK in the magnetic field applied along the [100] axis (upper curves) and the [001] axis (lower curves) for the electrical current flowing along the [001] axis [00AWMW]. **(a)** Data obtained by conventional dc method; **(b)** data taken when sweeping the field continuously under a constant current. There is no tendency to saturation in $\Delta\rho/\rho(0)$ measured along the [100] direction, while $\Delta\rho/\rho(0)$ taken along [001] first saturates and then slightly decreases at high fields. The magnetoresisivity along both directions exhibits pronounced Shubnikov-de Haas oscillations, seen most clearly in panel **(b)**. See the corresponding fast Fourier transform spectra in Fig. 352.

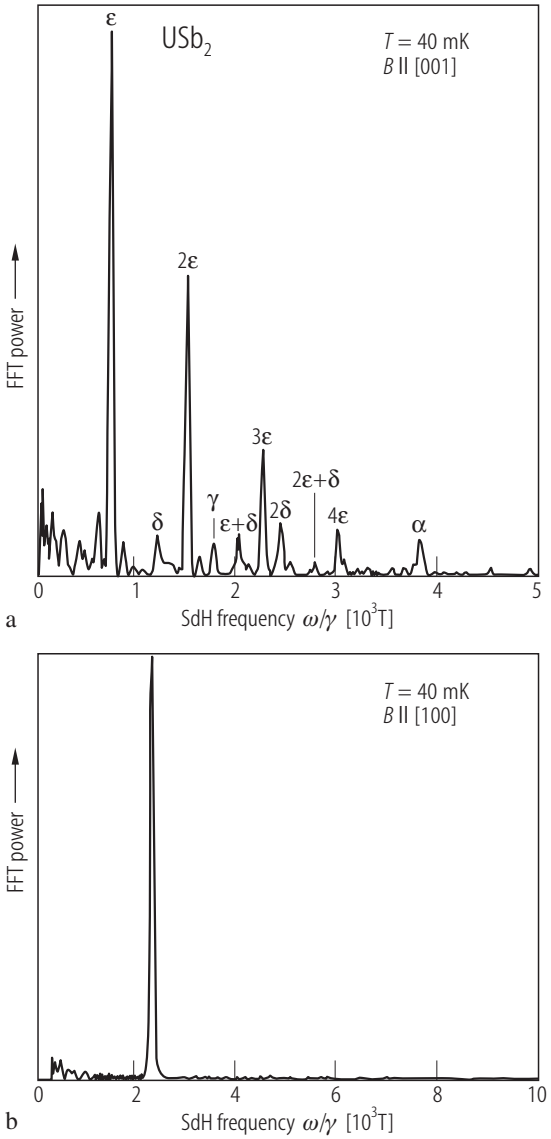

Fig. 352. USb_2, sc. Fast Fourier transform spectra corresponding to the Shubnikov-de Haas data from Fig. 350 [00AWMW]. **(a)** $B \parallel [001]$; **(b)** $B \parallel [100]$. Note the presence of four fundamental branches α, γ, δ and ε for the field along the [001] axis, and only one fundamental branch for the field along the [100] axis, in perfect agreement with de Haas-van Alphen results (compare Fig. 355).

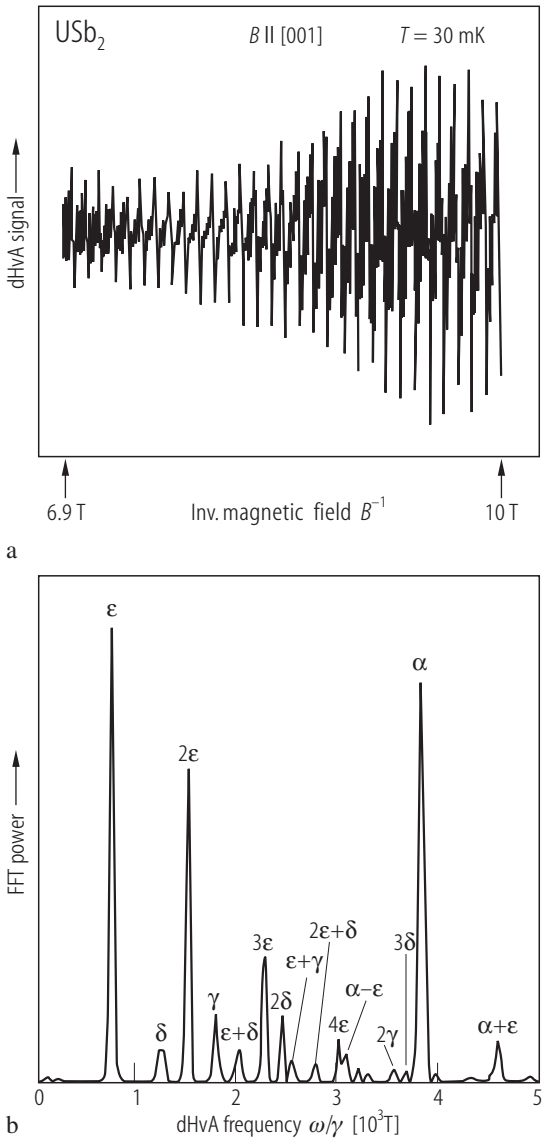

Fig. 353. USb_2, sc. **(a)** De Haas - van Alphen oscillations measured at $T = 30$ mK in magnetic fields ranging from 6.9 to 10 T applied along the [001] axis [00AWMW]. **(b)** Fast Fourier transform spectrum corresponding to the data from panel **(a)** [00AWMW]. Note the presence of four fundamental branches labeled α, γ, δ and ε in the frequency range from $7.6 \cdot 10^2$ to $3.82 \cdot 10^3$ T. The other features are higher harmonics. For the angular dependence of the dHvA frequencies see Fig. 355.

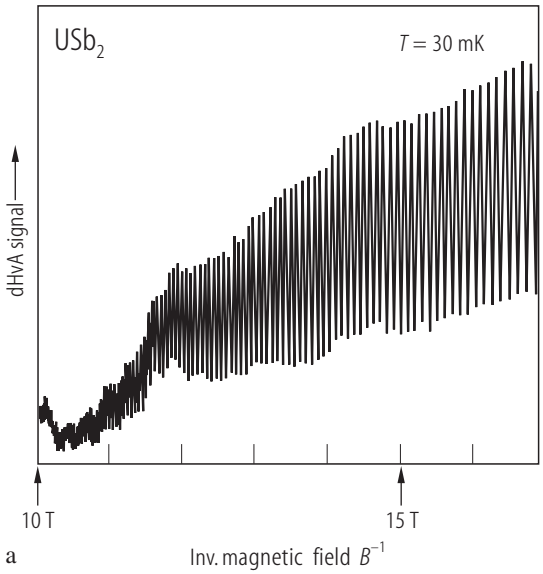

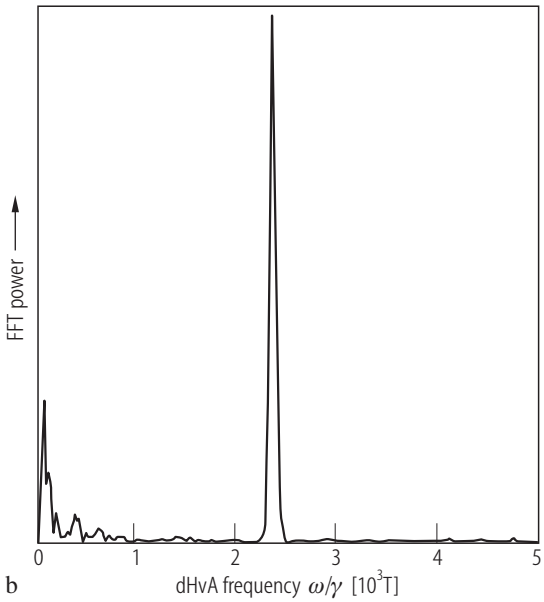

Fig. 354. USb_2, sc. **(a)** De Haas-van Alphen oscillations measured at T = 30 mK in magnetic fields B ranging from 10 to 15 T tilted by 7° from the [100] axis towards the [110] direction [00AWMW]. **(b)** Fast Fourier transform spectrum corresponding to the data from panel **(a)** [00AWMW]. Only one fundamental branch is observed at a frequency of $2.33 \cdot 10^3$ T (see also Fig. 355).

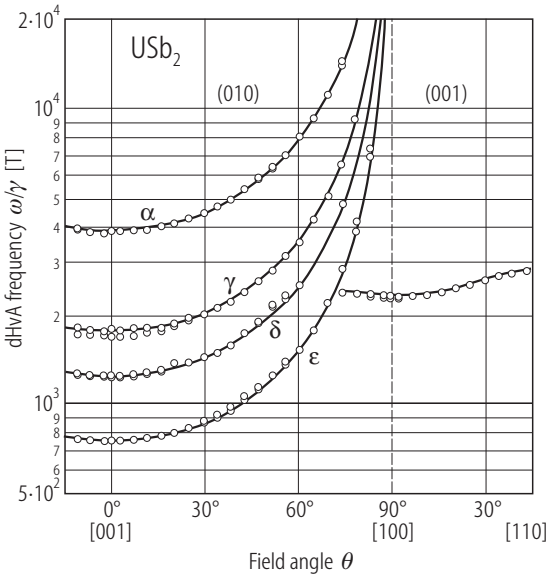

Fig. 355. USb_2, sc. Angular dependence of the dHvA frequencies measured as in Figs. 353 and 354 [00AWMW]. The solid line marks a $1/\cos\theta$ dependence for the branches α, γ, δ and ε, indicating the Fermi surface of cylindrical form (see Fig. 321). The branch ε follows this dependence up to 83.5°. Note that another branch appears in the (001) plane, which is almost independent of the field angle. This branch probably originates from the branches δ and ε via the magnetic breakthrough effect (for explanation see the original paper). The detected cyclotron mass for this branch is as large as 31 m_0 being close to the value expected from the effective mass model. For the other branches the effective cyclotron masses range from 2.0 to 6.0 m_0 (see Table L).

For Figs. 356, 357 see next page

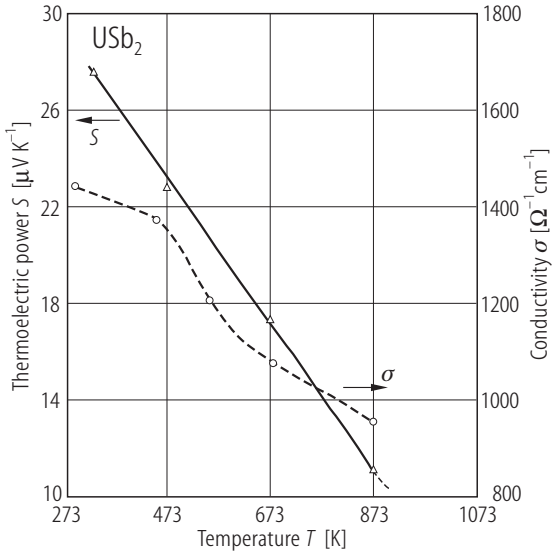

→

Fig. 358. USb_2. Thermoelectric power, S, (open triangles; left-hand scale) and electrical conductivity, σ, (circles; right-hand scale) vs. temperature, T, in the range 320…870 K and 273…870 K, respectively [64WP2].

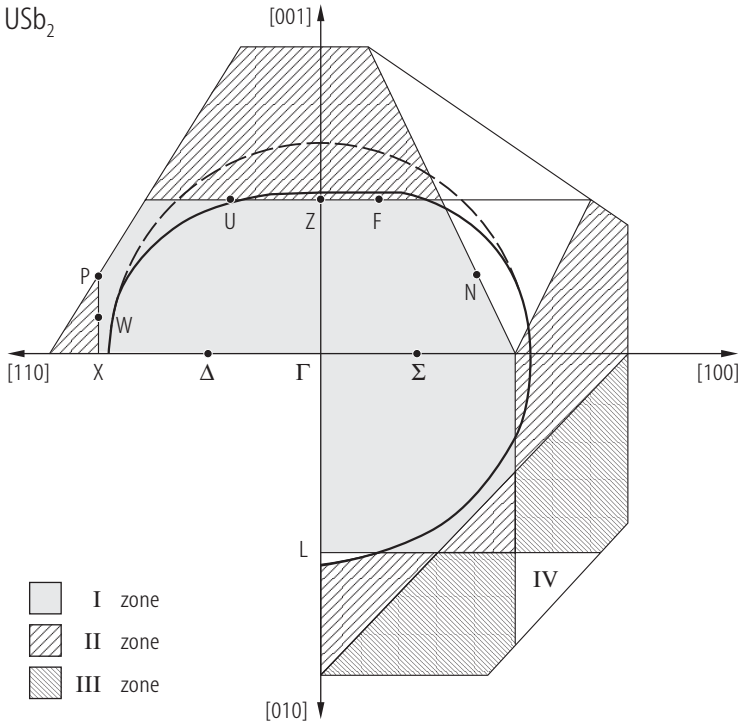

Fig. 356. USb_2. Cross-sections through the Brillouin zones and Fermi surface as derived from the calculated electron momentum density distributions $\rho(p)$ on the basis of the results of the positron annihilation experiments presented in Fig. 289 [80DR]. The dashed curves denote free-electron Fermi sphere. Note an ellipsoidal shape of the Fermi surface flattened in the [001] direction, which is in line with the observed anisotropy in the electrical resistivity (see Fig. 348) as well as with the results of dHvA and SdH studies (see Fig. 321).

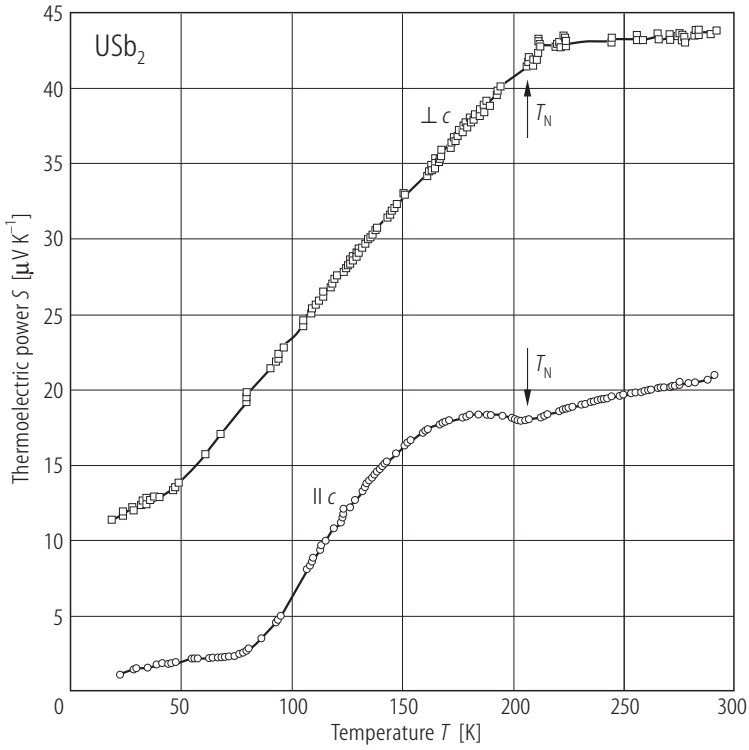

Fig. 357. USb_2, sc. Thermoelectric power, S, vs. temperature, T, measured along the c-axis (circles) and in the (ab)-plane (squares) [02TBSP]. Note that the thermopower is anisotropic in both paramagnetic and ordered regions although not so strongly as the resistivity (see Fig. 349). The results in the (ab)-plane are similar to the data reported by [92HMWF] but S(T) along the c-axis differs markedly from the previous findings.

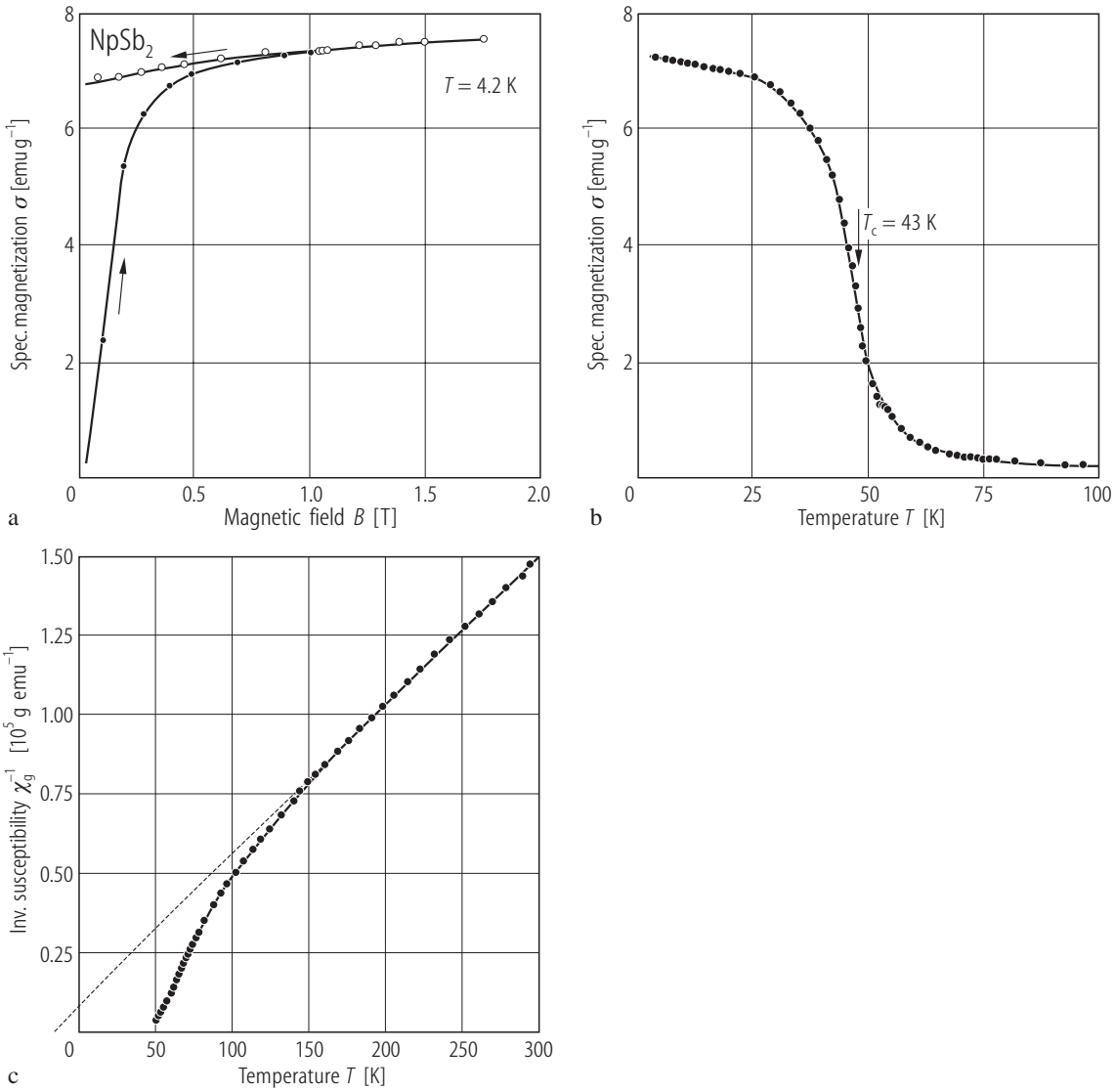

Fig. 359. $NpSb_2$. **(a)** Specific magnetization, σ, vs. magnetic field, B, taken at T = 4.2 K with increasing (full circles) and decreasing (open circles) magnetic field [82BFDC]. The saturation neptunium magnetic moment p_s = 0.65 μ_B is only 1/3 that value derived from the Mössbauer data [81BCAK]. Apart from the polycrystalline sample used, this discrepancy can hint to the presence of a noncollinear magnetic structure. **(b)** Specific magnetization, σ, vs. temperature, T, in the range 2…100 K measured in a field of 0.82 T [82BFDC]. T_C = 45 K. Below 25 K, $\sigma(T)$ follows a $T^{3/2}$ law (not shown). **(c)** Inverse mass magnetic susceptibility, χ_g^{-1}, vs. temperature, T [82BFDC]. The dashed line is a Curie-Weiss fit with the parameters given in Table F. p_{eff} = 2.87 μ_B is close to the value expected for a Np^{3+} ion within an intermediate coupling scheme (p_{eff} = 2.83 μ_B). Pronounced curvature of $\chi_g^{-1}(T)$ below 170 K evidences strong crystal field effects.

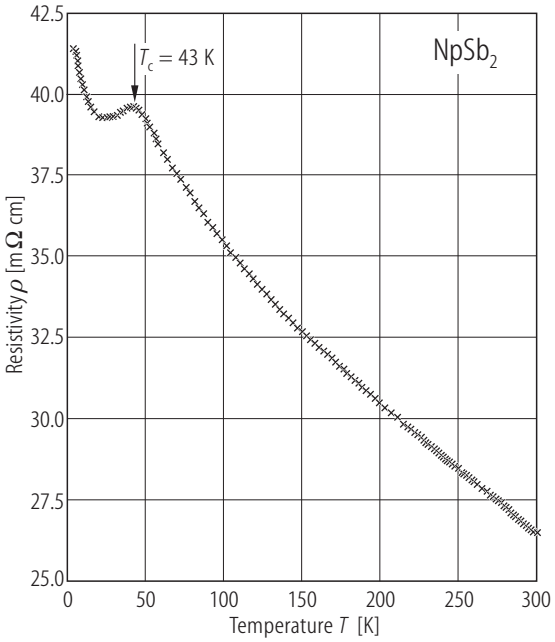

Fig. 360. $NpSb_2$. Electrical resistivity, ρ, vs. temperature, T [82BFDC]. Note a Kondo-like behaviour. A broad maximum at 43 K corresponds to the ferromagnetic phase transition (see Fig. 359). An increase in the resistivity below 20 K has unknown origin.

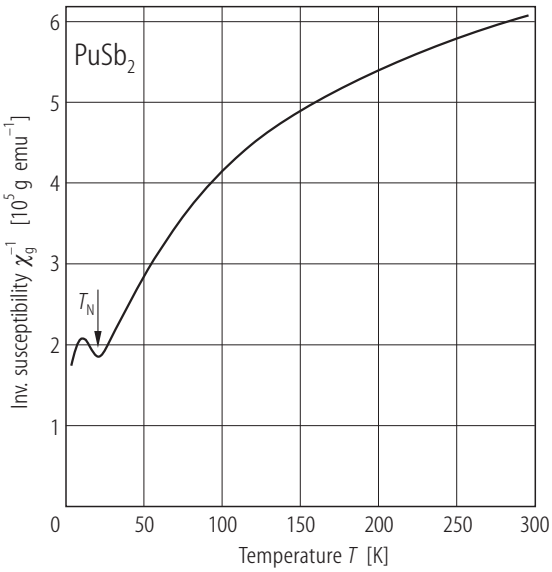

Fig. 361. $PuSb_2$. Inverse mass magnetic susceptibility, χ_g^{-1}, vs. temperature, T, measured in a field of 0.82 T [82BFD]. The compound orders antiferromagnetically at T_N = 21 K. The susceptibility exhibits some rise below 18 K, which was attributed to a change in the magnetic structure. In the paramagnetic region $\chi_g^{-1}(T)$ is strongly curvilinear and follows a modified Curie-Weiss law with the parameters given in Table F. p_{eff} = 0.75 μ_B indicates that Pu ions are trivalent (in Russell-Saunders coupling scheme the $5f^5$ configuration of Pu^{3+} gives p_{eff} = 0.845 μ_B).

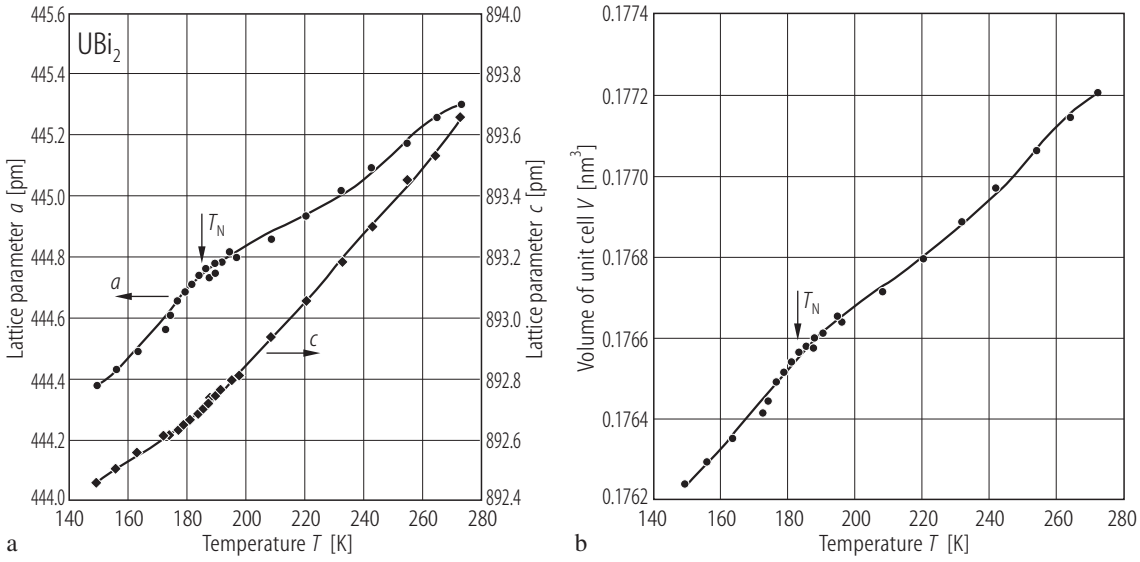

Fig. 362. UBi_2, sc. **(a)** Tetragonal lattice parameters, a and c, vs. temperature T, in the range 150…270 K [77PL]. Note changes in the slopes of $a(T)$ and $c(T)$ at the Néel temperature T_N = 181 K. **(b)** Unit cell volume, V, vs. temperature T [77PL].

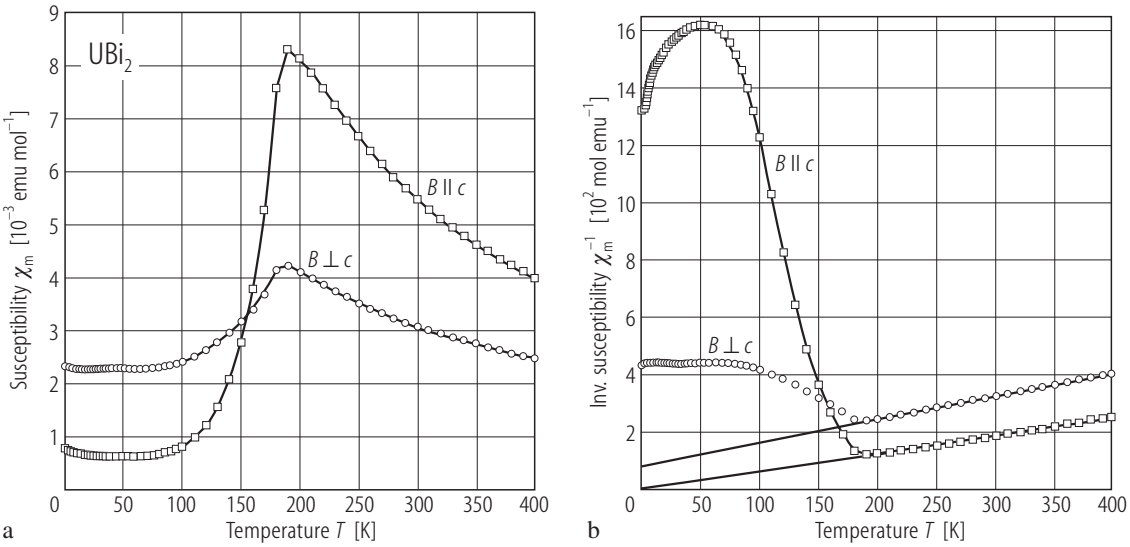

Fig. 363. UBi_2, sc. **(a)** Molar magnetic susceptibility, χ_m, vs. temperature, T, in the range 1.7…400 K, measured along the *c*-axis (open squares) and in the (*ab*)-plane (open circles) [02TSKP]. The compound orders antiferromagnetically at T_N = 181 K. **(b)** Inverse molar magnetic susceptibility, χ_m^{-1}, vs. T, measured as in panel **(a)** [02TSKP]. The solid lines are Curie-Weiss fits with the parameters given in Table F.

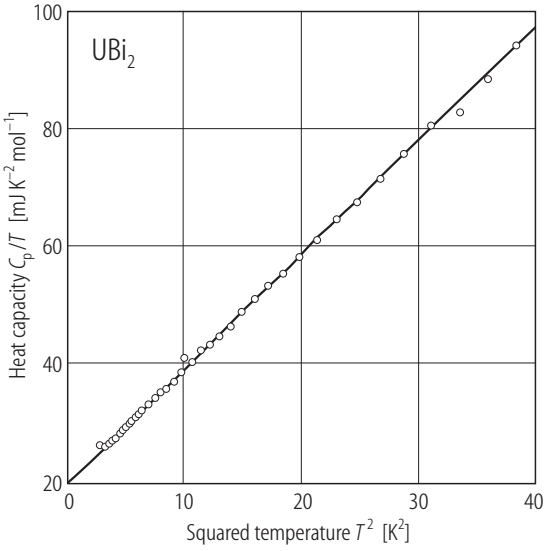

Fig. 364. UBi_2. Heat capacity over temperature, C_p/T, vs. squared temperature, T^2, in the range 1.5…6 K [00AWMW]. The solid line is a fit to the expression $C/T = \gamma(0) + \beta T^2$ yielding $\gamma(0)$ = 20 mJ/mol K^2.

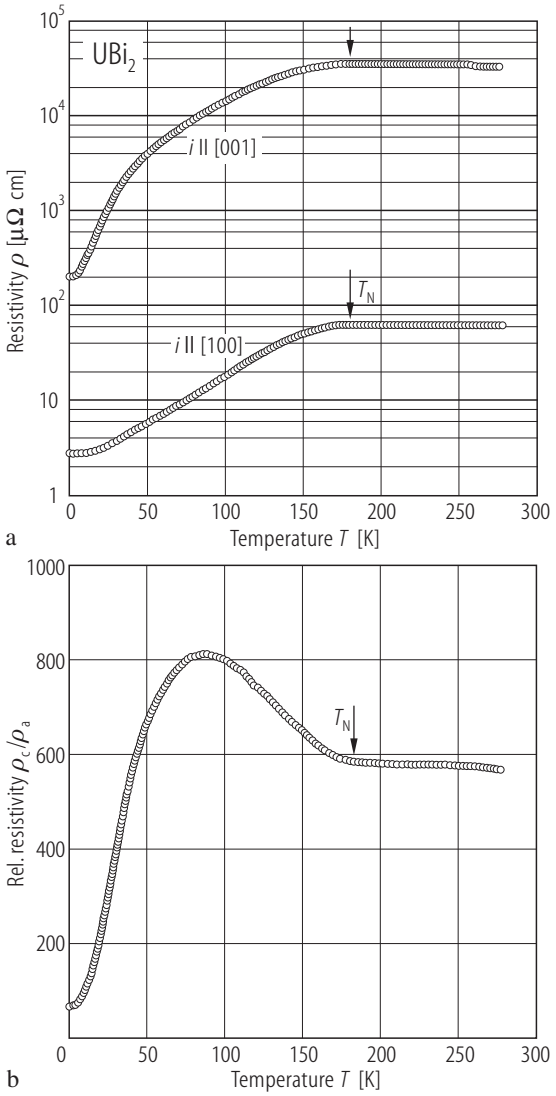

Fig. 365. UBi_2, sc. **(a)** Electrical resistivity, ρ, vs. temperature, T, down to 0.1 K measured with the current flowing along the [100] (ρ_a, lower curve) and [001] (ρ_c, upper curve) directions [00AWMW]. RRR is 180 along [001] and 22 along [100]. The arrows mark the antiferromagnetic phase transition at T_N = 181 K. **(b)** The anisotropy ratio, ρ_c/ρ_a, vs. T [00AWMW]. The resistivity anisotropy is extremely large (ρ_c/ρ_a reaches its maximum of 820 at about 80 K) indicating a quasi-two-dimensional behaviour of conduction. For the resistivity behaviour below T_N see also Fig. 301.

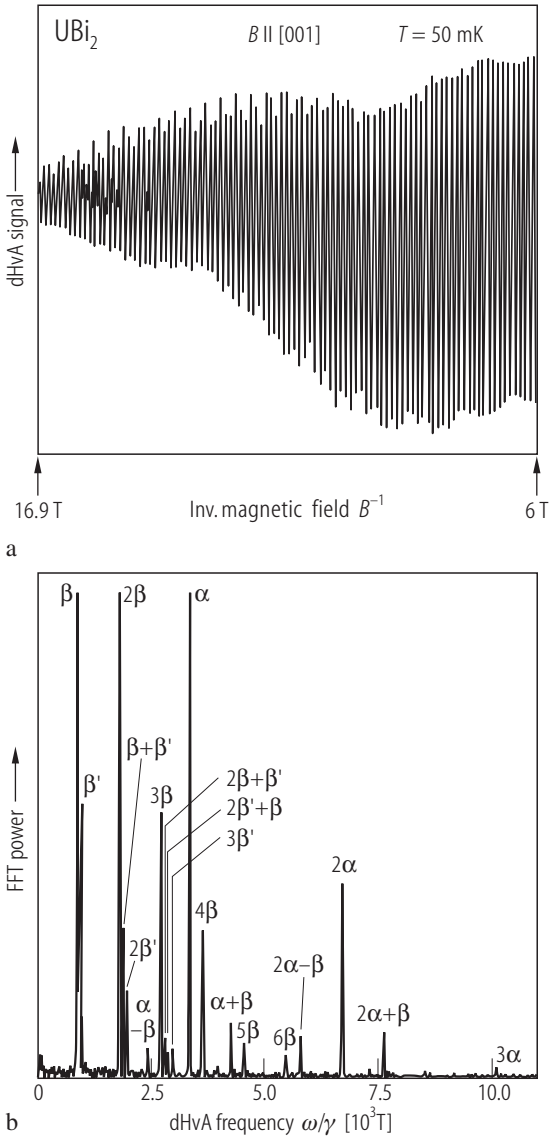

Fig. 366. UBi_2, sc. **(a)** De Haas-van Alphen oscillations measured at T = 50 mK in magnetic fields ranging from 6 to 16.9 T and applied along the [001] axis [00AWMW]. **(b)** Fast Fourier transform spectrum corresponding to the data from panel **(a)** [00AWMW]. Note the presence of two fundamental branches labeled α and β in the frequency range from $9.1 \cdot 10^2$ to $3.36 \cdot 10^3$ T. The branch β' originates from the same Fermi surface as the branch β, which is cylindrical but slightly corrugated (see Fig. 321). The other features are higher harmonics. For the angular dependence of the dHvA frequencies see Fig. 368.

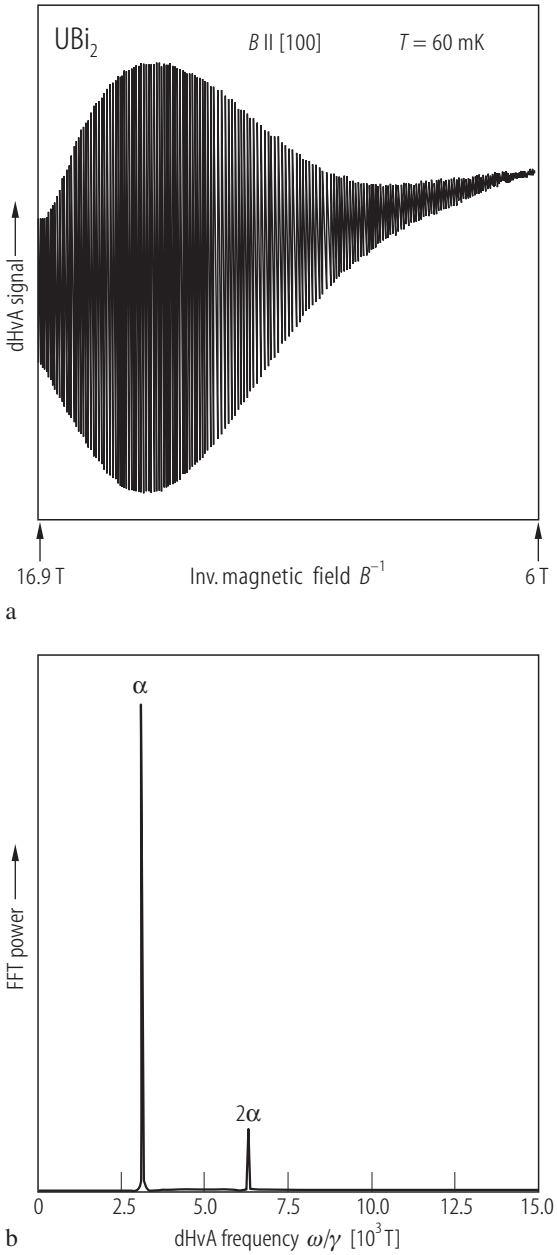

Fig. 367. UBi_2, sc. **(a)** De Haas - van Alphen oscillations measured at $T = 60$ mK in the magnetic field ranging from 6 to 16.9 T applied along the [100] axis [00AWMW]. **(b)** Fast Fourier transform spectrum corresponding to the data from panel **(a)** [00AWMW]. Note the presence of only one fundamental branch labeled α and its higher harmonics. For the angular dependence of the dHvA frequencies see Fig. 368.

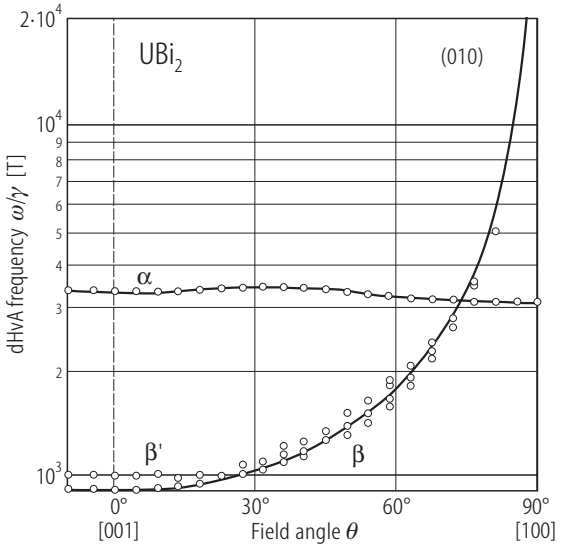

Fig. 368. UBi_2, sc. Angular dependence of the dHvA frequencies measured as in Figs. 366 and 367 [00AWMW]. The solid line marks a $1/\cos\theta$ variation for the branch β or β', indicating the Fermi surface of cylindrical form. The branch α is almost independent of the field angle, which indicates a nearly spherical Fermi surface (see Fig. 321). The effective cyclotron masses are 4.4 m_0, 6.3 m_0 and 9.2 m_0, for the branches β, β' and α, respectively (see also Table L). For further details refer to the original papers.

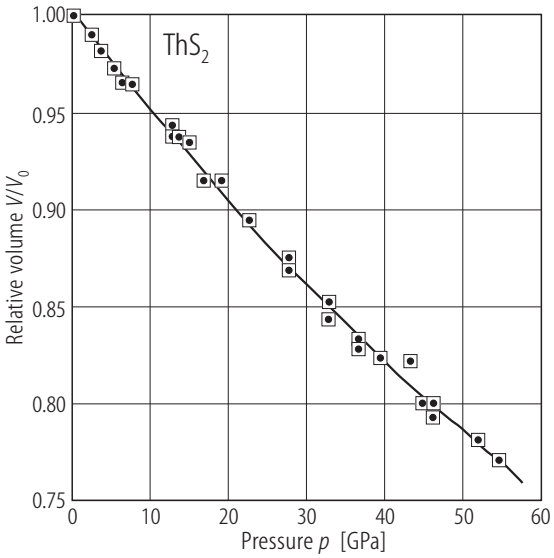

Fig. 369. ThS_2. Relative volume, V/V_0, vs. pressure, p, up to 55 GPa [93GSBD]. The solid curve was calculated from the equation of state. $B_0 = 195(15)$ GPa, $B_0' = 2(1)$. At about 50 GPa there occurs a first-order phase transformation from the orthorhombic $PbCl_2$-type structure to a high-pressure structure of unknown symmetry (this transition is not seen in the figure).

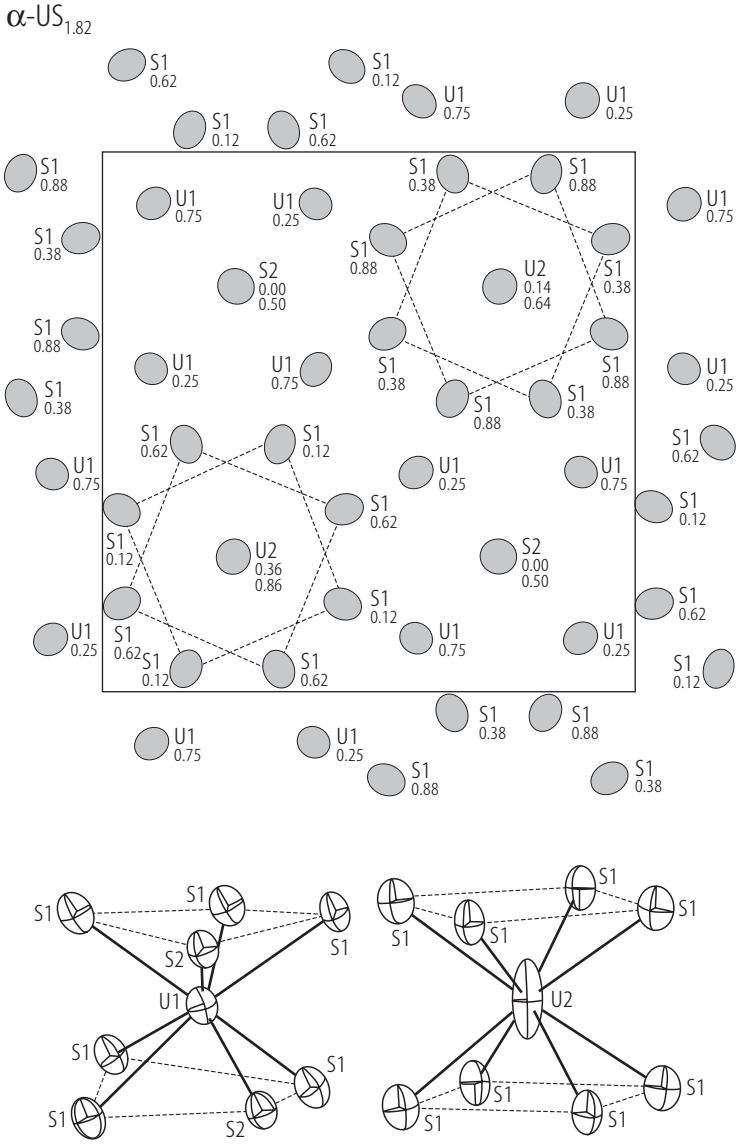

Fig. 370. α-US$_{1.82}$. Tetragonal crystal structure (space group P4/ncc) projected on the (*ab*)-plane [84NL]. Uranium atoms occupy two sites: U1 at 8(f) and U2 at 4(c). The nonstoichiometry is caused by incomplete filling of the 4(c) sites: approximately three U2 atoms are randomly distributed over four 4(c) sites yielding the S/U ratio of 1.82, in agreement with [68GHTT]. The deviation from ideal stoichiometry makes a formal valence of uranium equal to 3.6. The dotted lines represent a regular square antiprismatic coordination sphere of U2 atoms. The U1 atoms are bonded to eight S atoms forming a distorted antiprismatic polyhedron. Both coordinations are shown in the bottom of the figure.

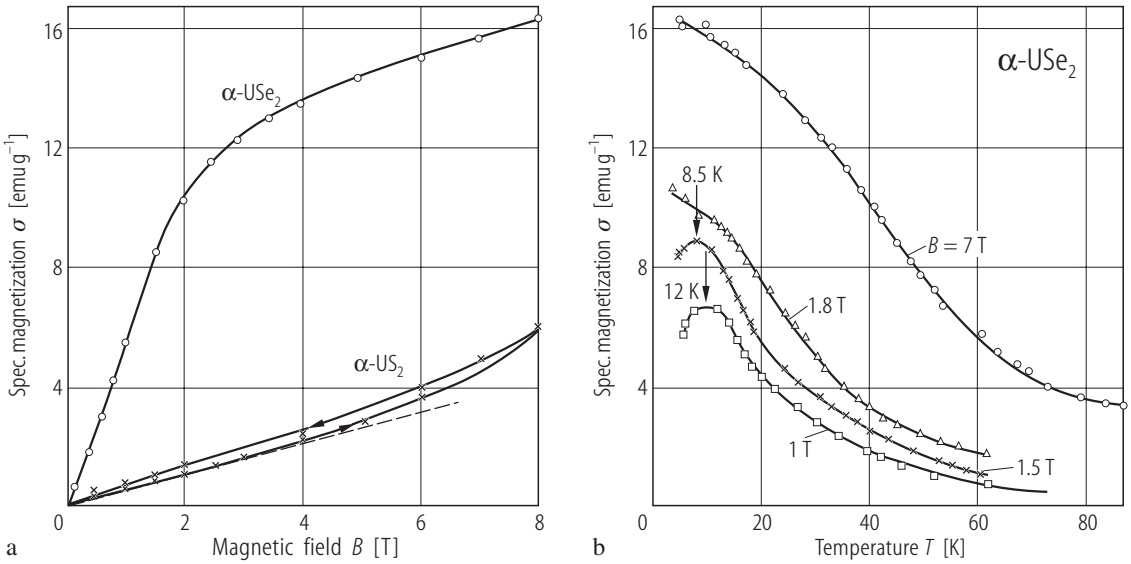

Fig. 371. α-UY_2, Y = S, Se. **(a)** Specific magnetization, σ, vs. magnetic field, B, up to 8 T taken at T = 4.2 K [72SCM]. For α-US_2 the measurements were made with increasing and decreasing magnetic field as indicated by the arrows. Note for this compound a metamagnetic–like transition above about 3 T, manifesting itself as a deviation from the dashed straight line. The other compound is probably also a metamagnet but with very small critical magnetic field. **(b)** Specific magnetization, σ, vs. temperature, T, for α-USe_2 taken in several different magnetic fields from 1 to 7 T [72SCM]. The maximum in $\sigma(T)$ at T_{max} = 12 K seen in B = 1 T disappears rapidly in a field as low as 1.8 T.

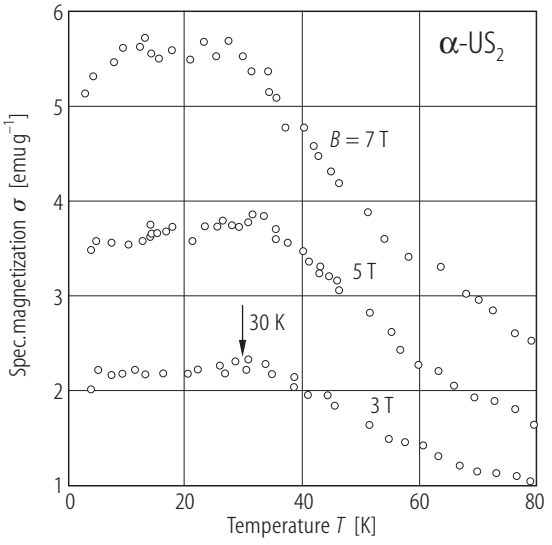

Fig. 372. α-US_2. Specific magnetization, σ, vs. temperature, T, taken in three different magnetic fields [72SCM]. A maximum in $\sigma(T)$ occurring at about 30 K finds its correspondence in an anomaly in the resistivity behaviour (see Figs. 377 and 378), however the low-temperature heat capacity is featureless (see Fig. 375).

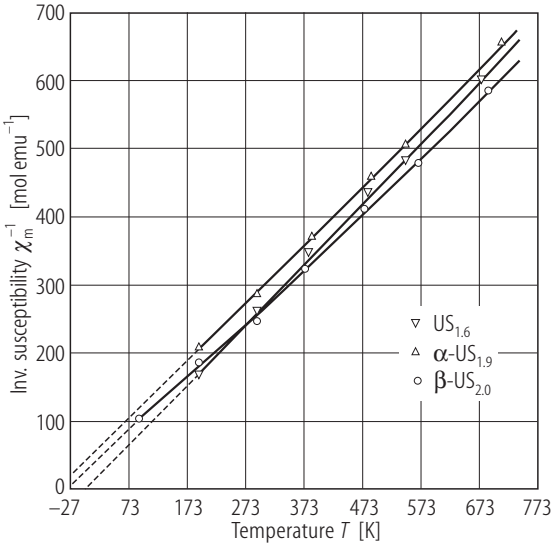

Fig. 374. US_{2-x}. Inverse molar magnetic susceptibility, χ_m^{-1}, vs. temperature, T, in the range 80…750 K [68GHTT]. Triangles down: $US_{1.6}$ (U_3S_5); triangles up: α-$US_{1.9}$; circles: β-$US_{2.0}$. The lines are Curie-Weiss fits with p_{eff} = 3.07 and 3.14 μ_B for α-$US_{1.9}$ and β-$US_{2.0}$, respectively.

For Fig. 373 see next page

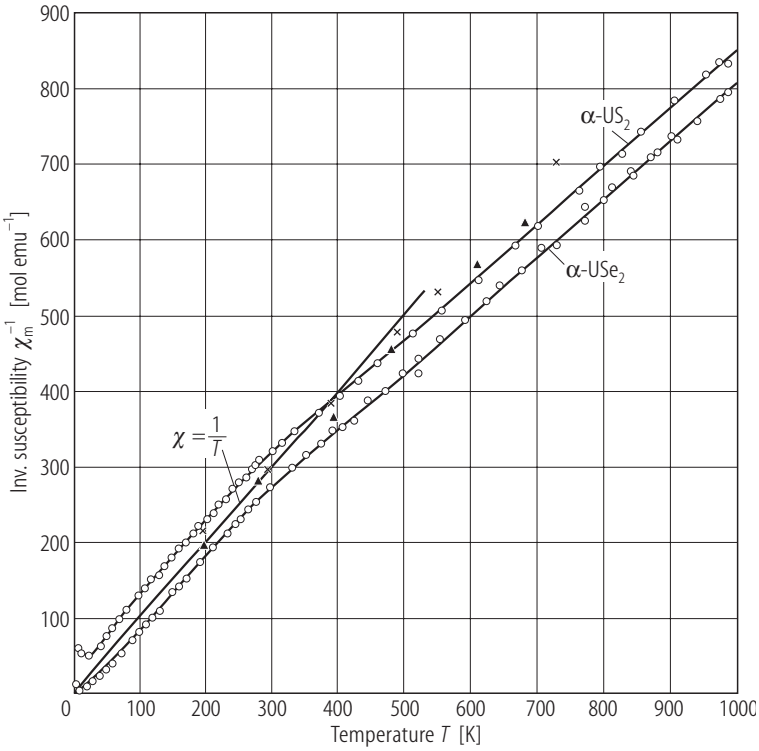

Fig. 373. α-UY_2, Y = S, Se. Inverse molar magnetic susceptibility, χ_m^{-1}, vs. temperature, T, in the range 4.2…1000 K (open circles) [72SCM, 73S]. The straight line represents a Curie law with $p_{eff} = 2.83$ μ_B. For comparison the data obtained for US_2 and USe_2 by [68GHTT] are shown by crosses and full triangles, respectively. In the latter study a little higher value for p_{eff} was determined for $80 < T < 700$ K (see Fig. 374).

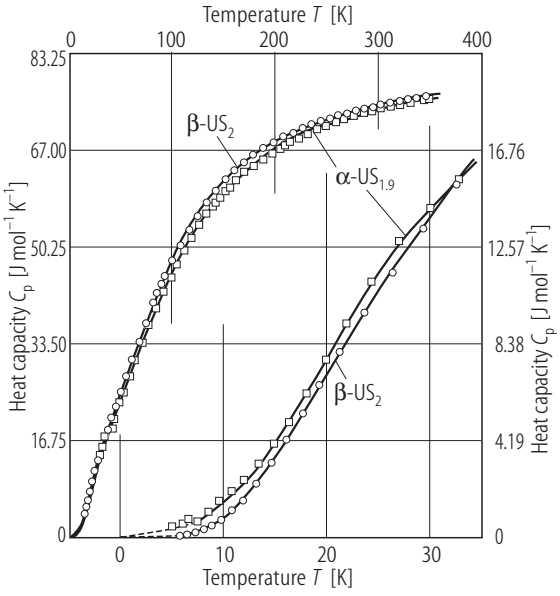

Fig. 375. US_{2-x}. Heat capacity, C_p, vs. temperature, T, in the range 5…350 K (upper and left-hand side scales) and 5…30 K (bottom and right-hand side scales) [70WG]. Open squares: α-$US_{1.9}$; open circles: β-$US_{2.0}$. For any of these two sulphides a phase transition was not found.

For Fig. 376 see next page

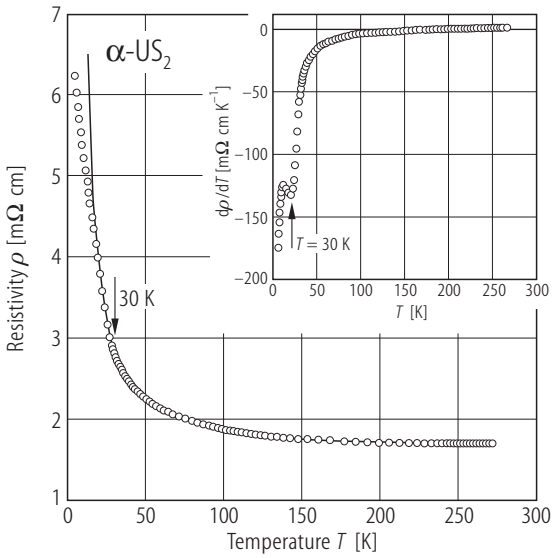

Fig. 377. α-US_2, sc. Electrical resistivity, ρ, vs. temperature, T, measured for the current flowing along the c-axis [95S, 99ST]. The solid line is a fit of the experimental data between 30 and 300 K to the equation $\rho(T)[\text{m}\Omega\text{cm}] = 1.6 \exp(3.1\,\text{meV} / 2k_B T)$. The energy gap $E_g = 3.1$ meV inferred in the paramagnetic range changes to 0.3 meV (see Fig. 378) in the ordered (probably antiferromagnetic) state. Inset: temperature derivative of the resistivity, $d\rho/dT$ vs. T in the vicinity of 30 K, where a clear anomaly occurs.

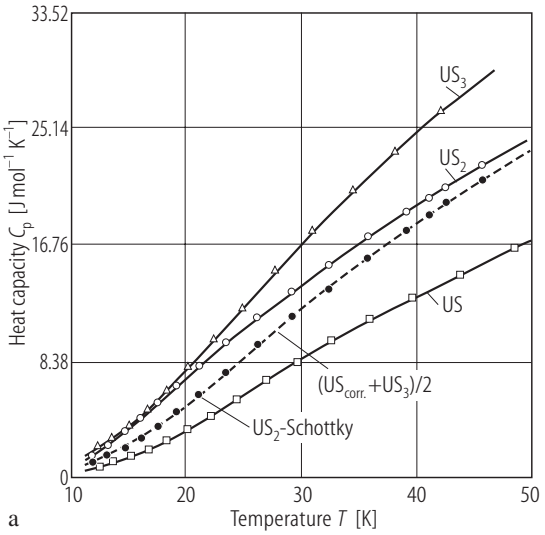

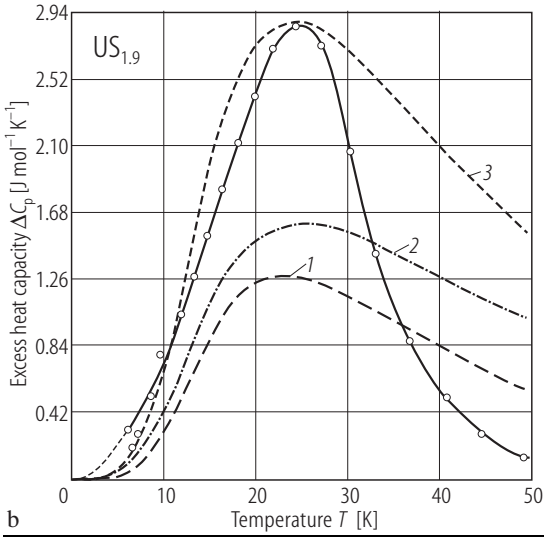

← **Fig. 376**. α-US$_2$. **(a)** Heat capacity, C_p, vs. temperature, T, in the range 12…45 K (open circles), compared with the data for US (open squares) and US$_3$ (open triangles) [68GW]. US$_{corr.}$ is the lattice heat capacity in US, obtained after subtracting the spin wave and conduction electrons contributions. The comparison indicates the presence of a Schottky type contribution to the specific heat of α-US$_2$ with a maximum of about 2.1 J/(mol K) at 25 K. **(b)** Excess heat capacity (open circles) [70WG]. Curve *1* is the contribution originated from one-fifth of the uranium atoms, which are surrounded by 8 sulfur atoms at the corners of a right antiprism. It was assumed that these U atoms have a singlet ground state and a doublet excited state ($g_1/g_0 = 2$) separated by $\Delta E/k_B = 68$ K. Curve *2* is the contribution from the other four-fifth U atoms, which have a doublet ground state and a singlet excited state ($g_1/g_0 = 1/2$) separated by $\Delta E/k_B = 56$ K. Curve *3* is the sum of these two contributions. Note that the above analysis is based on the crystal structure proposed for α-US$_{1.9}$ by [64M], i.e for s.g. I4/mcm. Another crystal structure of this compound with s.g. P4/ncc, determined by [84NL], is shown in Fig. 370. Even lower symmetry s.g.. P4/n was proposed by [89BD1] (see Fig. 380).

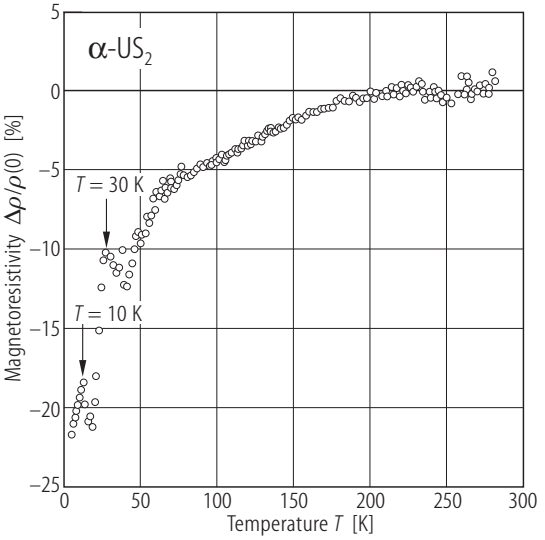

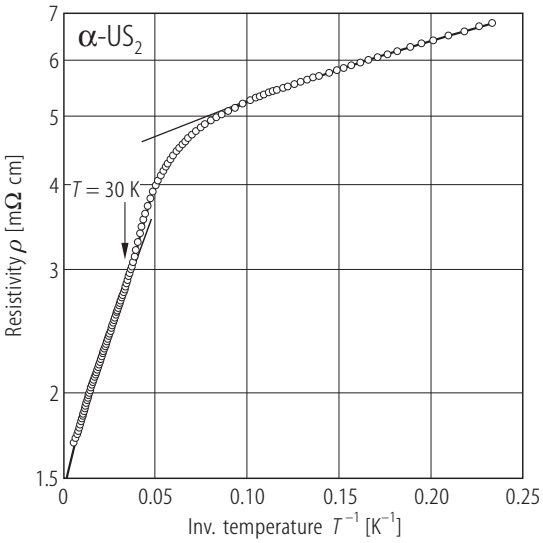

Fig. 378. α-US$_2$, sc. Electrical resistivity, ρ, vs. inverse temperature, $1/T$, measured for the current flowing along the *c*-axis [95S, 99ST]. The two solid lines represent the fits to the equations: $\rho(T)[\text{m}\Omega\text{cm}] = 1.6\exp(3.1\text{ meV}/2k_BT)$ in the range 30… 300 K and $\rho(T)[\text{m}\Omega\text{cm}] = 4.3\exp(0.3\text{ meV}/2k_BT)$ in the range 4.2…20 K.

← **Fig. 379**. α-US$_2$, sc. Magnetoresistivity, $\Delta\rho/\rho(0)$, vs. temperature, T, measured for the current flowing along the *c*-axis and the magnetic field of 1 T applied perpendicular to this axis [95S, 99ST]. Note a large value of –22% at 4.2 K and the presence of two negative maxima at $T = 10$ and 30 K. Nearly at the same temperatures two maxima were observed in $\sigma(T)$ (see Fig. 372). The origin of these anomalies is not known. Interestingly the magnetoresistivity becomes zero not earlier than as so high temperature as about 200 K.